

中央大学博士論文

Dielectric Permittivity Estimation at Microwave Frequencies

NGUYEN NGOC AN

博士（工学）

中央大学大学院 理工学研究科 情報セキュリティ科学専攻

Chuo University

Graduate School of Science and Engineering

Information Security Sciences Course

March 2017

Table of Contents

1	Introduction	1
1.1	Background	1
1.2	Thesis contents	3
2	Some introductions on dielectric permittivity and estimation methods	5
2.1	Dielectric permittivity of materials	5
2.2	Current permittivity estimation methods	8
2.3	Free space methods for dielectric permittivity estimation	9
2.3.1	Current free space methods	9
2.3.2	Introduction of a new free space method and the required scattering analysis	10
3	High frequency electromagnetic scattering analysis of rectangular dielectric cuboids	12
3.1	Introduction	12
3.2	Scattering formulation by Kirchhoff approximation	15
3.3	Scattering from rectangular PEC cuboids	19
3.4	Scattering from rectangular dielectric cuboids	26
3.5	Conclusions	32
4	Dielectric permittivity estimation for solid materials using free space method	33

4.1	The relation between the complex relative dielectric permittivity, the multiple reflection coefficient and the complex scattering quantity . . .	34
4.2	Permittivity estimation method	38
4.3	Requirements of the method	43
4.4	Measurements and discussions	47
4.5	Conclusions	56
5	Dielectric permittivity estimation for liquids	57
5.1	Introduction	58
5.2	Scattering analysis	59
5.2.1	Some differences compared to the case of a solid material . . .	59
5.2.2	The decomposition of the scattering container	60
5.2.3	Scattering analysis and validation	60
5.3	Permittivity estimation	74
5.4	Measurements and discussions	75
5.4.1	Water's relative permittivity	75
5.4.2	Container's relative permittivity	75
5.5	Conclusions	81
6	Concluding remarks	82
	Acknowledgment	85
	References	86
	List of Publications	90

List of Figures

1.1	The potentials of dielectric permittivity measurement in some applications.	2
2.1	Some common types of dielectric polarization.	6
2.2	The effect of permittivity on capacitance.	7
2.3	Some current dielectric permittivity measurement methods.	7
3.1	Scattering from a rectangular dielectric cuboid.	14
3.2	Monostatic RCS of thin conducting plate S1 ($\phi = \phi_0 = 90^\circ$). (a) —: this method (=PO); ---: GTD single diff.; - · - · - : HFSS; ·····: measured (b) Thickness consideration —: $2c = 0.5$ mm; ·····: $2c = 0$ mm	22
3.3	Monostatic RCS of conducting cuboid S2 ($\phi = \phi_0 = 90^\circ$).	23
3.4	Monostatic RCS of aluminum cube S3 ($\phi = \phi_0 = 90^\circ$).	23
3.5	Bistatic RCS of thin aluminum plate S1 ($\phi_0 = 90^\circ, \theta_0 = 45^\circ$).	24
3.6	Bistatic RCS of aluminum cuboid S2 ($\phi_0 = 90^\circ, \theta_0 = 45^\circ$).	24
3.7	Bistatic RCS of aluminum cube S3 ($\phi_0 = 90^\circ, \theta_0 = 45^\circ$).	25
3.8	Range S_n of the departing rays r_n after n-time internal reflection in yOz plane.	26
3.9	Monostatic RCS of the polymer cuboid S4 ($\phi = \phi_0 = 90^\circ, 24$ GHz). (a) —: this method; ---: surface reflection only; - · - : collective approximation. (b) —: this method; ·····: measured; - · - · - : HFSS.	29

3.10	Monostatic RCS of the polymer material S5 ($\phi = \phi_0 = 90^\circ$, 24 GHz). (a) —: this method; - - -: surface reflection only; -·-: collective approximation. (b) —: this method; ·····: measured; - · - · - : HFSS.	30
3.11	Monostatic RCS of the polymer material S6 ($\phi = \phi_0 = 90^\circ$, 19.5 GHz). (a) —: this method; - - -: surface reflection only; -·-: collective approximation. (b) —: this method; ·····: measured; - · - · - : HFSS.	31
4.1	TE polarized plane wave scattering from a rectangular dielectric cuboid at the normal incidence.	36
4.2	Monostatic RCS of a nylon cuboid in the frequency domain ($2a = 2b = 100.0$ mm, $2c = 29.0$ mm). The relative permittivity $\varepsilon_r (= 3.023 + i0.043)$ is assumed to be the average value measured by the open-ended coaxial probe method given in Table 4.1.	37
4.3	Schematic diagram of the measurement configuration.	37
4.4	Example of least squares approximation of the real part of $\bar{\Gamma}_s$ from the multiple reflection coefficient Γ_m	41
4.5	Approximation of the real parts of the multiple reflection coefficients of a 21-mm thick dielectric slab, $\varepsilon_r = 3.00 + i0.01$	41
4.6	Approximation of the real parts of the multiple reflection coefficients of a 21-mm thick dielectric slab, $\varepsilon_r = 100.00 + i0.01$	42
4.7	Least squares approximation of the real part of $\bar{\Gamma}_s$ from the measured multiple reflection coefficient Γ_m of a Macor cuboid ($2a = 2b = 100.0$ mm, $2c = 30.0$ mm).	42
4.8	An example of the differences between the approximated reflection coefficients and the true surface reflection coefficient.	46
4.9	Relative permittivity estimations at different thicknesses of nylon and colored acrylic slabs.	46

4.10	Relative permittivity ε_r extracted from a nylon cuboid ($2a = 2b = 100.0$ mm, $2c = 29.0$ mm) at 23.0°C	49
4.11	Relative permittivity ε_r extracted from an acrylic cuboid ($2a = 2b = 100.0$ mm, $2c = 30.0$ mm) at 23.0°C	50
4.12	Relative permittivity ε_r extracted from a Macor ceramic cuboid ($2a = 2b = 100.0$ mm, $2c = 30.0$ mm) at 21.0°C	51
4.13	Percent cumulative probability distribution of the real part of the relative permittivity of measured acrylic sample.	52
4.14	Percent cumulative probability distribution of the imaginary part of the relative permittivity of measured acrylic sample.	52
4.15	Percent cumulative probability distribution of the real part of the relative permittivity of measured Macor ceramic sample.	53
4.16	Percent cumulative probability distribution of the imaginary part of the relative permittivity of measured Macor ceramic sample.	53
4.17	Percent cumulative probability distribution of the real part of the relative permittivity of measured nylon sample.	54
4.18	Percent cumulative probability distribution of the imaginary part of the relative permittivity of measured nylon sample.	54
4.19	Relative permittivities extracted from a rubber cuboid.	55
4.20	Relative permittivities extracted from a glass cuboid cuboid.	55
4.21	ε_r extracted from a wood cuboid ($2a = 2b = 2c = 120.0$ mm).	56
5.1	Scattering model for the liquid container.	65
5.2	Multiple-layer dielectric structures for scattering analysis.	66
5.3	Complex relative permittivities of container's material and water at 22°C	67
5.4	Debye model of the relative permittivity of water at 22°C by Stogryn in a comparison with contemporary results [37].	68
5.5	Complex far field scattering quantities of each container's part and total contribution.	69

5.6	A comparison with measurement.	70
5.7	The complex scattering quantity of a container filled with air.	71
5.8	Reduced model of the center part of the container.	72
5.9	Effects of the thickness b on the real part of the reflection coefficient of the center part ($l = w = 100.0$ mm, $a = 1.0$ mm) of a container. . .	73
5.10	Effects of the thickness b on the imaginary part of the reflection co- efficient of the center part ($l = w = 100.0$ mm, $a = 1.0$ mm) of a container.	73
5.11	Permittivity estimation process.	74
5.12	The real container used for measurement.	76
5.13	Theoretical and extracted complex far field scattering quantities of the center part- Case I.	77
5.14	Complex relative permittivity of water estimated from the partially filled container- Case I.	78
5.15	Complex relative permittivity of water estimated from the fully filled container- Case II.	79
5.16	Complex relative permittivity of acrylic estimated from the partially filled container.	80

List of Tables

2.1	Permittivity estimation models used in free space methods for solid materials	11
3.1	List of materials under test	18
4.1	Sample materials and their relative permittivities	48
5.1	Dimensions of the components of the container	63

Chapter 1

Introduction

1.1 Background

In general, substances can be categorized into three groups, namely dielectrics, semi-conductors and conductors in terms of the ability to allow electric currents to travel through [1]. Dielectrics or insulators are materials which do not conduct electric currents or have very low conductivity. Meanwhile, conductors allow electric current to flow easily. Dielectric materials show their presence everywhere in our daily life. They are the insulators that protect us from electric currents, the concrete and bricks that built our houses, the wood in our furniture, the leather of our shoes, the fabric of our clothes, the food that we eat and even the air that we breath.

The dielectric permittivity is a parameter that draws very much attentions of researchers and the industries. The main reason is that knowing the permittivity or how it changes at certain frequencies provides us with information that sheds insights and creates many important applications in various disciplines. For example, knowing the change in complex permittivity of wine allows authorities to quickly investigate the quality and composition of liquids [2]. Understandings on soil, clay, rock and various plants' permittivities are crucial for earth science, agriculture production and even the oil industry in several important application such as drought prediction, landslide prevention and oil field management, and etc. [3, 4]. Another

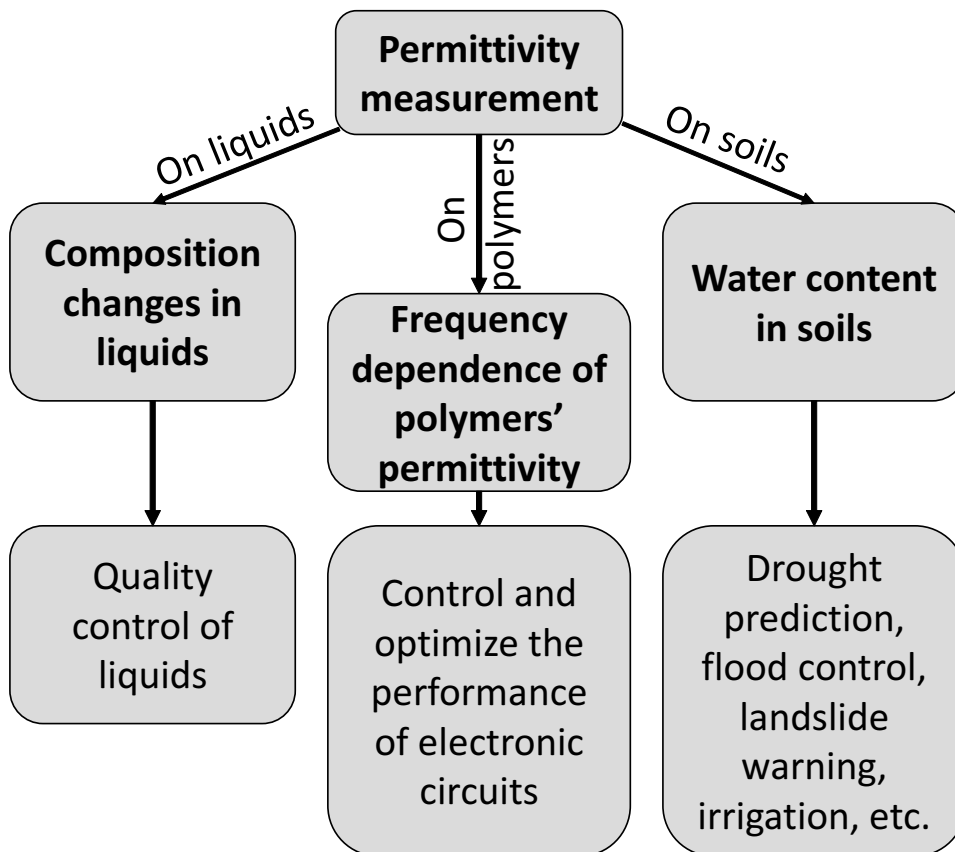


Figure 1.1: The potentials of dielectric permittivity measurement in some applications.

material example that can highlight the importance of knowing the dielectric permittivity is polymers. Polymers are revolutionary materials. They are important and are the main ingredients to make insulators, the base of electronic circuits and RF circuits and etc. Therefore, understanding the dielectric properties of plastics has been an important part of material science [5]. Such examples can be numerous but all of them confirm the paramount importance of permittivity estimation and lead to the development of many methods in past several decades [1]. Although there have been several methods developed to estimate the dielectric permittivity of materials, each method has its own advantages and disadvantages as will be explained with more details in Chapter 2. Furthermore, with recent advances in sciences and industries, knowing the frequency-dependent dielectric properties of materials at a wide range of microwave frequencies has become a more and more important re-

quirement in several industrial applications and various disciplines of science such as electromagnetics, chemistry, material science, biology, water studies, and etc. To fulfill the requirement, this research aims to develop a fast, broadband technique to estimate relative permittivity of solid materials and water-based liquids. The output technique is expected to be robust and able to make contactless, nondestructive estimations. This research also offers new approaches to solve the difficulty in permittivity estimation that current methods are facing. Promising results were obtained.

1.2 Thesis contents

This thesis consists of six chapters.

In Chapter 2, some basics on dielectric property of material are explained. A brief review on some main methods of permittivity estimation is also presented showing the advantages and disadvantage of each category. Taking the advantage of the group of the free space methods, my method of permittivity estimation is introduced to overcome the difficulties that the conventional free space methods struggle. My method is based on an electromagnetic scattering analysis using high frequency technique.

In Chapter 3, the electromagnetic scattering analysis that make the foundation of my estimation method is explained. The analysis is based on a high frequency technique called Kirchhoff approximation using reflected wave. The theoretical derivation is shown and verified by several comparisons with experiments and reference methods. Good agreements were confirmed with both PEC and dielectric scatterers. In the case of dielectric cuboids, a ray tracing technique has been used to estimate quite accurately the scattering far field.

In Chapter 4, the analysis established in Chapter 3 is summarized to emphasis the relation between the scattering quantity and the dielectric permittivity of solid materials. The relation is further analyzed to devise an iterative process in order to extract the relative permittivity from the measured data. An algorithm was

developed to calculate for the relative permittivity without knowing much about the material's dielectric property in advance. The proposed methods were applied on several material samples. Dielectric permittivities were successfully estimated and compared to the results by another method and references. Good agreements were observed.

Chapter 5 is an expansion into the realm of water and water-based liquids. Since liquids need containers, the effect from a container needs to be included in the scattering analysis. A decomposition was proposed to separate the unwanted scattering contributions from the measured scattering quantities. Based on the theory developed in Chapter 3, the validity of the proposed decomposition was confirmed. Based on the structure of the container and the lossy nature of water in liquids, two reflection coefficient models are proposed to calculate the scattering quantities and to establish a direct analytic relation between the dielectric permittivity of water and known information. Later, a procedure for dielectric permittivity estimation on water and water-based liquids is described. The procedure is verified by estimating water permittivity from an acrylic container and inversely. The results contain measurement errors so they oscillate, however the average values agree well with references. Further improvements are required to increase accuracy.

Finally, Chapter 6 shows some conclusions and discussions on future prospects of the estimation process. In the following chapters, a time harmonic factor $e^{-i\omega t}$ is assumed and suppressed throughout the context.

Chapter 2

Some introductions on dielectric permittivity and estimation methods

2.1 Dielectric permittivity of materials

The dielectric permittivity is an intrinsic parameter of a dielectric material that represents the capacity to store electrical energy of the material. Various authors [1, 6, 7] have introduced very comprehensive and thorough introductions on the definition and significance of this quantity. Therefore, I would like to summarize just some basics information to provide a simple grasp on this important parameter.

While conductors and semiconductors have the free electric charges, dielectrics or insulators have bound charges, constrained by atomic and molecular forces. When an electric field is applied on a dielectric material, the bound charges cannot travel freely but can only change their positions a little creating polarization in accordance to the field direction. That means a net amount or dipole moment or energy is stored inside the dielectric volume. The effect of an external electric field on the polarization of material is illustrated in Fig. 2.1. To further illustrate the idea, we consider the

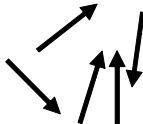
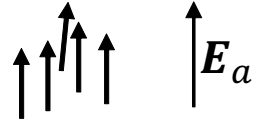
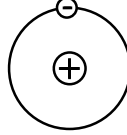
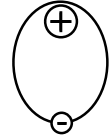
Mechanism	No applied field	With applied field
Dipole or orientational polarization		
Electronic polarization		

Figure 2.1: Some common types of dielectric polarization.

case of two large conducting plates placed in parallel with one another in vacuum so that the distance between the two plates are much smaller than the dimensions of the plates. The same amount of charges with opposite signs are placed on each side. This is the configuration of a vacuum capacitor, represented by a capacitance C_0 . When we replace the entire vacuum environment by a dielectric medium, the capacitance will change to a new value C_1 . The proportion between C_1 and C_0 gives us a quantity named the static dielectric permittivity of the material. In practice, a capacitor has small dimensions, so that other effects can prevent us from obtaining the dielectric permittivity exactly. The effect of permittivity on the capacitance of a capacitor is shown in Fig. 2.2.

When a dielectric material is exposed to an electric field that varies in time, the orientation of electric charges in the material also will change in accordance with the applied field. For the polar dielectrics, the re-orientation of the electric charges inside the material may not keep pace with the reversal of the electric field, thus induces loss in the form of heat inside the material. To account for energy loss in the material, the imaginary part of permittivity ε'' is defined. Meanwhile, ε' is the real part of permittivity that represents the capacity to store energy in the material.

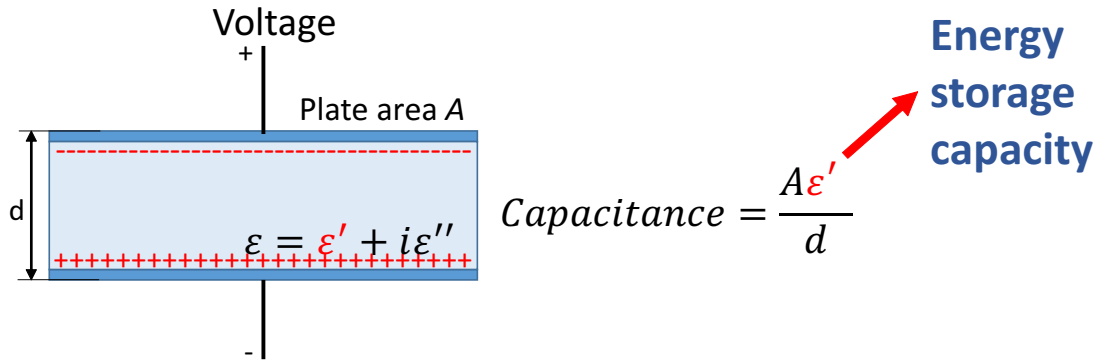


Figure 2.2: The effect of permittivity on capacitance.

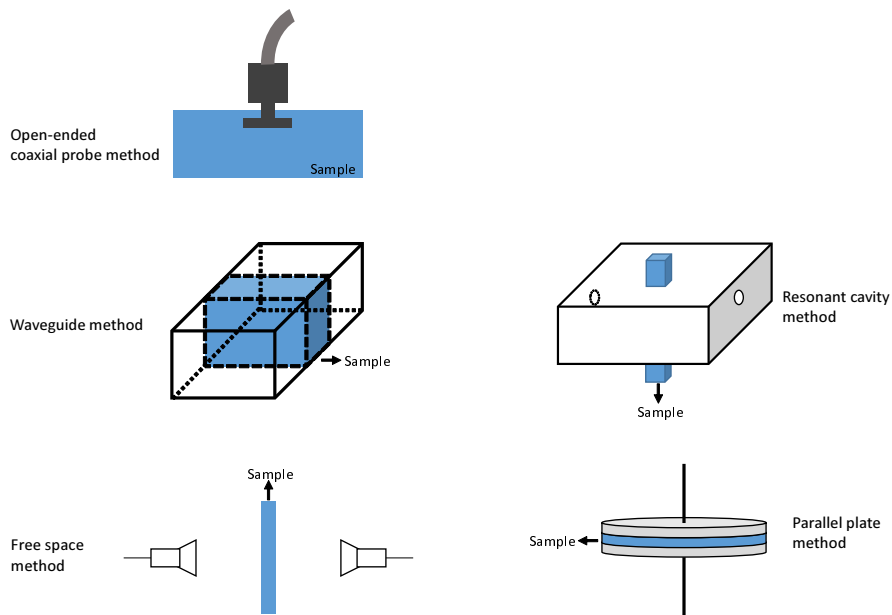


Figure 2.3: Some current dielectric permittivity measurement methods.

Therefore, the dielectric permittivity is described in complex form by

$$\epsilon = \epsilon' + i\epsilon'' = \epsilon_0\epsilon'_r + i\epsilon_0\epsilon''_r. \quad (2.1)$$

Here, ϵ_0 is the dielectric permittivity of vacuum. $\epsilon_r = (\epsilon'_r, \epsilon''_r)$ is the complex relative permittivity of the material. The complex permittivity of a material is a characteristic that depends on frequency.

2.2 Current permittivity estimation methods

Various measurement methods designed for different materials, frequencies and other requirements have been reviewed extensively and thoroughly by many authors [1, 8, 9, 10, 11, 12, 13]. Well-known techniques are the capacitor, the resonant cavity, the open resonator, the waveguide, the coaxial probe and the free space methods. The configurations of some of the common methods can be seen in Fig. 2.3. These methods can be divided broadly into two groups of techniques, namely the resonance methods and the transmission line methods [13].

The resonance methods are capable of conducting nondestructive measurements of very low loss materials with high accuracy. However, measurements can be made at only narrow frequency bands or separate frequencies [13].

The transmission line methods, on the other hand, are able to make fast, broadband measurements and are capable of measuring medium and high permittivity [13]. In this group, the waveguide methods, the open-ended coaxial probe methods and the free space transmission and/or reflection methods are well known. The waveguide methods are known for high accuracy and are suitable for high and medium loss materials [12, 13]. There are some difficulties, however, from the facts that they require fine preparation of the sample materials and highly accurate positioning. Among this group, the open-ended coaxial probe method is versatile, simple and easy to use. This method has, on the other hand, some limiting factors. Firstly, a perfect contact between the probe facet and the sample material needs to be guaranteed. For liquid or semi-solid materials, it may be easy. But for solid materials, this condition requires not only fine polishing on the sample's surface, but also extreme positioning care to maintain a good contact during the measurement. Secondly, a direct contact between the probe and the material surface may create scratches which may reduce the measurement accuracy.

Given the increasing need of broadband, non-destructive, non-contacting material characterization in material science and electronics, as well as in large scale environment monitoring systems, the traditional methods face several limits. In this

context, the free space techniques emerge as a powerful solution with many striking features. They allow broadband measurements, safely reserve the material sample and they are capable of assessing the material from afar or under extreme conditions.

2.3 Free space methods for dielectric permittivity estimation

2.3.1 Current free space methods

The abilities of the free space methods have been verified by several authors with different variations [14, 15, 16, 17]. These authors used various settings and parameters to estimate the relative permittivities and permeabilities. For example, they have used two S-parameters, samples with different thicknesses, PEC plate termination, time domain gating technique and measurement at the Brewster angle. Efforts have been made to improve the estimation accuracy.

In general, these techniques will face an ambiguity in determining the true value of the relative permittivity, since there are numerous complex permittivity values which satisfy the equation of the reflection/transmission coefficient as described by Redheffer [8] and Hasar [18].

The problem is often fixed by limiting the sample thickness, knowing the range of permittivity in advance or measuring with different initial conditions, etc. However, these measures are rather laborious and inconvenient. Additionally, people often use more than one S-parameter in the conventional permittivity estimation using the transmission measurements. However, this practice requires more equipment, which may cause more uncertainty than when only the reflection parameter is used. Currently, solving this difficulty requires laborious procedures and reduces convenience. Therefore, a new free space method to solve this difficulty is meaningful in the research perspective and will improve industrial efficiency. This new method is the purpose of this research.

2.3.2 Introduction of a new free space method and the required scattering analysis

The need of a new free space method to improve efficiency and convenience is the main motivation of this research. In this study, we shall propose a free space method to find the relative permittivity of non-magnetic dielectric samples from the monostatic complex scattering quantity in the specular reflection direction. This quantity is defined in a way that gives a direct analytical calculation of the complex surface reflection coefficient which, in turn, leads us to the desired permittivity by using our proposed estimation process.

In the case of solid material, our free space method uses an algorithm to find automatically the appropriate initial guesses for the relative permittivity, avoiding the difficulty of the multi-valued selection. In the cases of water and water-based liquids, an analytical formula is presented to determine the dielectric permittivity approximately in a direct manner. My estimation is based on only the reflection coefficient S_{11} , while the transmission coefficient S_{21} is not used. Additional conditions, such as fixing the sample length, measurements with different configurations, or knowing the range of the relative permittivity in advance, are not used. Therefore, measurement complexity is reduced and convenience is increased in comparison to other free space methods. Typical free space methods are summarized in Table 2.1.

Our estimation formulation is based on the following assumptions.

- 1) The material under test is homogeneous and isotropic.
- 2) The sample has an electrically large cubic shape.
- 3) In case of solid material, its relative permittivity could be weakly frequency-dispersive and could be approximated by a linear curve.

The validity of our approaches has been verified by comparisons with the open-ended coaxial probe method and other references. Good agreements have been observed for nylon and acrylic samples. An analysis was given to the limit of the method regarding sample thickness.

As can be found in the literature, the reflection coefficient is a conventional start-

Table 2.1: Permittivity estimation models used in free space methods for solid materials

Calculation model	Solution Type	Output	Parameters used	Required information	Initial guess	Comments
Our model	Iterative	ε_r	S_{11}	Non/weakly dispersive, non-magnetic material Sample dimensions, reference plane	Generated automatically	————
Nicholson-Ross Model [19]	Analytical	ε_r, μ_r	S_{11}, S_{21}	Sample length, reference plane	Not required	Unstable for the thickness of $n\lambda/2$. (n is a positive integer and λ is the wavelength inside the sample.)
NIST Model [20]	Iterative	ε_r	S_{11}, S_{12} S_{21}, S_{22}	Non-magnetic material Independent of sample length, reference plane	Unknown	The method needs to use 4 parameters so it requires more equipment. As a result, more measurement errors may be included.
Transmission Model [21]	Iterative	ε_r	S_{21}	Non-magnetic material Sample length, reference plane	Usually $\varepsilon_r = 1 + i0.0$	The initial guesses may be located too far from the physical relative permittivity value. Thus, estimation may be time consuming or converges to unwanted solutions.

ing point to solve for the relative dielectric permittivity. This coefficient can be determined by solving the scattering problem. To adopt the free space method, we have chosen to calculate the reflection coefficient by establishing an analytic formula between the reflection coefficient and the complex scattering quantity. This quantity will be explained in Chapter 4. The establishment of this relation is the same as solving for the scattering far field of the material sample and will be presented in Chapter 3.

Chapter 3

High frequency electromagnetic scattering analysis of rectangular dielectric cuboids

This chapter will explain the scattering analysis developed to calculate the scattering far field of a dielectric cuboid to build the basics of my permittivity estimation method. A background introduction and comparisons with measurements, simulations and other methods also will be given to show the novelty and validity of the scattering analysis.

3.1 Introduction

Field Equivalence theorem is one of the powerful tools to analyze the radiation and the scattered fields in electromagnetic theory [22, 23]. While the method provides us with an exact field solution when the equivalent currents are derived from the exact field, the method also works pretty well to predict the scattering field by using only a primary constituent of the field. Huygens' principle could be the original idea for such equivalent sources for secondary waves and Kirchhoff's approach, which is

sometimes referred as Physical Optics (PO) approximation, provides a reasonably accurate estimation of the diffraction field when the scattering object is electrically large [24, 25].

PO is a powerful method in dealing with PEC bodies, and is widely applied in scattering estimation as well as in antenna design. Ever since the original PO formulation was introduced, many modifications have been proposed to obtain more accurate diffraction fields. Physical Theory of Diffraction (PTD), proposed by Ufimtsev, is one of the well known extensions to correct field behaviors near the rim or the edge of conducting scatterers by introducing a fringe wave [26]. Some works have been developed in conjunction with the Method of Equivalent Currents (MEC) [27, 28, 29]. Most of them, however, are devoted for the conducting bodies and few are related with dielectric ones. In dealing with conducting scatterers, one might also apply the Geometrical Theory of Diffraction (GTD), which describes the field as a sum of diffracted rays [30]. While GTD utilizes the diffraction coefficient of the local scattering feature, which may be obtained by solving the canonical problems, difficulties arise in the derivation of the appropriate coefficients for corner or dielectric wedge diffraction.

In this paper, a high frequency scattering field has been formulated using the Kirchhoff approximation for dielectric cuboids. As will be shown later, our formulation is closely related to the conventional PO method or aperture field integration method. The equivalent electric and magnetic currents have been derived here for the forward scattering field by the *reflected* electric and magnetic fields from the scatterer. This concept marks a key difference between our proposal and the conventional PO in which the equivalent current is derived from only the incident magnetic field component. Moreover, because of its own definition, the conventional PO is limited to calculations on conducting surfaces. Meanwhile, our method can postulate the equivalent currents on any fictitious surface between the scatterer and the observation point. In case of dielectric objects, these equivalent currents derived from the reflected waves partially take into account the effects of multiple reflec-

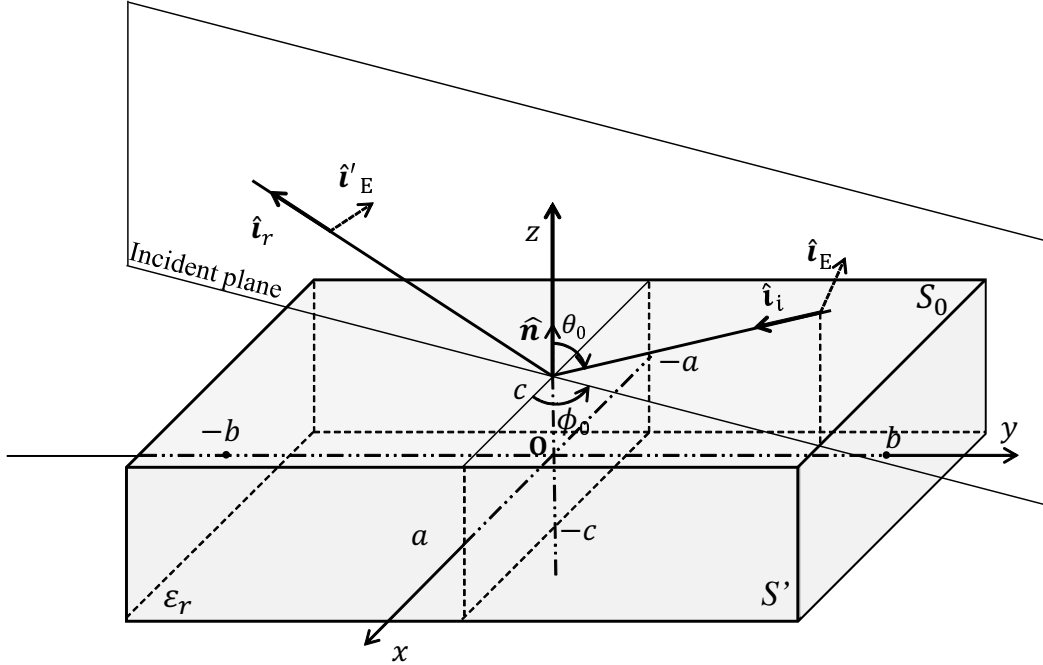


Figure 3.1: Scattering from a rectangular dielectric cuboid.

tion inside the object. Therefore, our method has a potential to explain scattering properties of not only PEC but also dielectric bodies.

Monostatic and bistatic radar cross sections (RCSs) of rectangular dielectric cuboids are calculated and compared with the results by other methods, such as PO, GTD, the HFSS simulation and experiments. Good agreement has been found confirming the validity of our method.

3.2 Scattering formulation by Kirchhoff approximation

Figure 3.1 demonstrates a case when a transverse electric (TE) polarized plane wave of the amplitude E_0 :

$$\mathbf{E}^i = E_0 \hat{\mathbf{i}}_E e^{ik\hat{\mathbf{i}}_i \cdot \mathbf{r}} \quad (3.1)$$

impinges upon a surface S' of a rectangular dielectric cuboid whose relative dielectric constant is ε_r and dimensions are $2a \times 2b \times 2c$. Here, the vectors $\hat{\mathbf{i}}_E$ and $\hat{\mathbf{i}}_i$ denote the unit polarization and propagation vectors of the incident wave, and k denotes the free space wave number.

The scattering far field may be calculated from radiation integrals from equivalent currents \mathbf{J}_{eq} , \mathbf{M}_{eq} due to the field on a postulated surface S_{eq} enclosing the scattering object. For high frequency field where the dimension of the scattering object is pretty large comparing with the wavelength, the main scattering field arises from the specular reflection of the incident wave. Accordingly, the equivalent currents \mathbf{J}_{eq} , \mathbf{M}_{eq} may be derived from the reflected wave. Let us choose the postulated surface S_{eq} to be the surface S' of the cuboid, and treat the contribution from each component facet separately.

For the top surface $S_0(-a \leq x \leq a, -b \leq y \leq b, z = c)$, the reflected electric and magnetic fields can be described as

$$\mathbf{E}^r = \Gamma_s(\theta_0) E_0 \hat{\mathbf{i}}'_E e^{-i2kc \cos \theta_0} e^{ik\hat{\mathbf{i}}_r \cdot \mathbf{r}}, \quad (3.2)$$

$$\mathbf{H}^r = \frac{1}{Z_0} \hat{\mathbf{i}}_r \times \mathbf{E}^r, \quad (3.3)$$

where \mathbf{r} , $\hat{\mathbf{i}}'_E$ and $\hat{\mathbf{i}}_r$ are the position vector of the observation point, the unit polarization and propagation vectors of the reflected wave, and Z_0 ($\approx 120\pi$) denotes the free space wave impedance. Following the Snell's law of reflection, one finds that $\hat{\mathbf{i}}_r = \hat{\mathbf{i}}_i - 2\hat{\mathbf{n}}(\hat{\mathbf{i}}_i \cdot \hat{\mathbf{n}})$ and $\hat{\mathbf{i}}'_E = \hat{\mathbf{i}}_E$ with the unit normal vector $\hat{\mathbf{n}}$ ($= \hat{\mathbf{z}}$). $\Gamma_s(\theta_0)$ represents the conventional reflection coefficient from the top surface, and

$$\Gamma_s(\theta_0) = \frac{\cos \theta_0 - \sqrt{\varepsilon_r - \sin^2 \theta_0}}{\cos \theta_0 + \sqrt{\varepsilon_r - \sin^2 \theta_0}} \quad (3.4)$$

is obtained from the dielectric interface at $z = c$ of two half spaces. When one considers a finite thickness and the multiple bouncing effect, the reflection coefficient may be modified as $\Gamma_m(\theta_0)$ in a collective form [31]:

$$\Gamma_m(\theta_0) = \frac{\Gamma_s(\theta_0)(1 - e^{i4kc\sqrt{\varepsilon_r - \sin^2 \theta_0}})}{1 - \Gamma_s^2(\theta_0)e^{i4kc\sqrt{\varepsilon_r - \sin^2 \theta_0}}}. \quad (3.5)$$

This $\Gamma_m(\theta_0)$ is valid only around the normal incident direction ($\theta_0 = 0^\circ$), and is invalid when the reflected surface is truncated at a finite size, as one sees later. Details on the derivation of this collective reflection coefficient in the normal direction can be found in Ref. [31].

Equivalent currents \mathbf{J}_{eq} , \mathbf{M}_{eq} may be found from the above reflected wave at $z = c$ as

$$\mathbf{J}_{eq} = \hat{\mathbf{n}} \times \mathbf{H}^r, \quad \mathbf{M}_{eq} = \mathbf{E}^r \times \hat{\mathbf{n}}. \quad (3.6)$$

Then the radiation electric fields due to these currents can be derived through electric and magnetic vector potentials \mathbf{A} and \mathbf{F} as [31]

$$\mathbf{E} = i\omega \mathbf{A} + \frac{i\omega}{k^2} \nabla(\nabla \cdot \mathbf{A}) - \frac{1}{\varepsilon_0} \nabla \times \mathbf{F}, \quad (3.7)$$

$$\mathbf{A} = \frac{\mu_0}{4\pi} \int_{S_0} \mathbf{J}_{eq}(\mathbf{r}') \frac{e^{ik|\mathbf{r}-\mathbf{r}'|}}{|\mathbf{r}-\mathbf{r}'|} dS', \quad (3.8)$$

$$\mathbf{F} = \frac{\varepsilon_0}{4\pi} \int_{S_0} \mathbf{M}_{eq}(\mathbf{r}') \frac{e^{ik|\mathbf{r}-\mathbf{r}'|}}{|\mathbf{r}-\mathbf{r}'|} dS', \quad (3.9)$$

where \mathbf{r}' denotes the position vector of the current source. Assuming that the observation point is far from the cuboid, one can use the far field approximation to execute the above integrals analytically. Without taking into account the multiple bouncing effect, the electric scattering far field from the top surface in a spherical

coordinate system (r, θ, ϕ) can be given as

$$\begin{aligned}
E_{\theta}^s &= -\frac{i}{k\pi} \Gamma_s(\theta_0) E_0 \frac{e^{ikr}}{r} e^{-ikc(\cos\theta_0 + \cos\theta)} (\cos\theta_0 \cos\theta + 1) \\
&\quad \cdot \sin(\phi - \phi_0) \frac{\sin[ka\{\sin\theta_0 \cos\phi_0 + \sin\theta \cos\phi\}]}{\sin\theta_0 \cos\phi_0 + \sin\theta \cos\phi} \\
&\quad \cdot \frac{\sin[kb\{\sin\theta_0 \sin\phi_0 + \sin\theta \sin\phi\}]}{\sin\theta_0 \sin\phi_0 + \sin\theta \sin\phi}, \tag{3.10}
\end{aligned}$$

$$\begin{aligned}
E_{\phi}^s &= -\frac{i}{k\pi} \Gamma_s(\theta_0) E_0 \frac{e^{ikr}}{r} e^{-ikc(\cos\theta_0 + \cos\theta)} (\cos\theta_0 + \cos\theta) \\
&\quad \cdot \cos(\phi - \phi_0) \frac{\sin[ka\{\sin\theta_0 \cos\phi_0 + \sin\theta \cos\phi\}]}{\sin\theta_0 \cos\phi_0 + \sin\theta \cos\phi} \\
&\quad \cdot \frac{\sin[kb\{\sin\theta_0 \sin\phi_0 + \sin\theta \sin\phi\}]}{\sin\theta_0 \sin\phi_0 + \sin\theta \sin\phi}. \tag{3.11}
\end{aligned}$$

One should note that the above results are only valid for $\theta \leq 90^\circ$. E_r^s is negligible. Similar contributions from the other surfaces of the cuboid should also be considered in the same manner, but the formulation is omitted here due to the limited space. In order to verify the accuracy of our method, Radar Cross Section (RCS) of several cuboids are calculated using the following definition.

$$\sigma_{3D} = \lim_{r \rightarrow \infty} 4\pi r^2 \frac{|\mathbf{E}^s|^2}{|\mathbf{E}^i|^2} \tag{3.12}$$

The obtained results are then compared with those by other methods and measurements. The list of targets is summarized in Table I. Treatment for the multiple bouncing effect will be described in the cases of dielectric cuboids.

Table 3.1: List of materials under test

Sample	Length $2a$ [mm]	Width $2b$ [mm]	Thickness $2c$ [mm]	Material ϵ_r	Frequency [GHz]
S1	100.0	100.0	0.5	Aluminum $\sigma \rightarrow \infty$	24.0
S2	100.5	100.5	8.2	Aluminum $\sigma \rightarrow \infty$	24.0
S3	100.0	101.1	101.1	Aluminum $\sigma \rightarrow \infty$	24.0
S4	100.0	150.0	53.7	Polymer $6.66 + 0.28i$	24.0
S5	100.1	100.1	40.7	Polymer $6.40 + 0.11i$	24.0
S6	101.9	100.5	100.7	Polymer $6.52 + 0.05i$	19.5

3.3 Scattering from rectangular PEC cuboids

Let us first discuss about the scattering from rectangular PEC cuboids. In this instance, $\Gamma_s(\theta_0)$ becomes -1 for all incident directions as taking the conductivity $\sigma \rightarrow \infty$. One should note the difference between our formulation and the conventional PO. The latter involves the current distribution

$$\mathbf{J}^{PO} = 2\hat{\mathbf{n}} \times \mathbf{H}^i \quad (3.13)$$

on the actual PEC surface. Therefore, the resultant scattering electric fields are excited only from the vector potential \mathbf{A} as

$$\begin{aligned} \bar{E}_\theta^s &= \frac{2i}{k\pi} E_0 \frac{e^{ikr}}{r} e^{-ikc(\cos\theta_0 + \cos\theta)} \cos\theta_0 \cos\theta \\ &\cdot \sin(\phi - \phi_0) \frac{\sin[ka\{\sin\theta_0 \cos\phi_0 + \sin\theta \cos\phi\}]}{\sin\theta_0 \cos\phi_0 + \sin\theta \cos\phi} \\ &\cdot \frac{\sin[kb\{\sin\theta_0 \sin\phi_0 + \sin\theta \sin\phi\}]}{\sin\theta_0 \sin\phi_0 + \sin\theta \sin\phi}, \end{aligned} \quad (3.14)$$

$$\begin{aligned} \bar{E}_\phi^s &= \frac{2i}{k\pi} E_0 \frac{e^{ikr}}{r} e^{-ikc(\cos\theta_0 + \cos\theta)} \cos\theta_0 \\ &\cdot \cos(\phi - \phi_0) \frac{\sin[ka\{\sin\theta_0 \cos\phi_0 + \sin\theta \cos\phi\}]}{\sin\theta_0 \cos\phi_0 + \sin\theta \cos\phi} \\ &\cdot \frac{\sin[kb\{\sin\theta_0 \sin\phi_0 + \sin\theta \sin\phi\}]}{\sin\theta_0 \sin\phi_0 + \sin\theta \sin\phi}. \end{aligned} \quad (3.15)$$

By comparing the results Eqs. (3.10), (3.11) with Eqs. (3.14), (3.15), one notices that some difference arises in the amplitude term as $-\Gamma_s(\theta_0)(\cos\theta_0 \cos\theta + 1) \rightarrow 2\cos\theta_0 \cos\theta$ in Eq. (3.14) and $-\Gamma_s(\theta_0)(\cos\theta_0 + \cos\theta) \rightarrow 2\cos\theta_0$ in Eq. (3.15), respectively. Thus, one can expect that our derived scattering solutions in Eqs. (3.10) and (3.11) behave like PO but with different oscillation amplitudes, and the accuracy would be similarly good as PO.

Monostatic and bistatic RCS of these PEC cuboids are calculated in the yOz plane ($\phi = \phi_0 = 90^\circ$) and compared with other methods in Figs. 3.2 ~ 3.7. It is obvious for the monostatic RCS calculation ($\theta = \theta_0$) from the analytical formula that E_θ^s in Eq. (3.10) vanishes and E_ϕ^s in Eq. (3.11) coincides with \bar{E}_ϕ^s in Eq. (3.15) by PO.

For large PEC objects, it is expected that GTD can predict well for the high frequency scattering waves by considering the edge diffraction. The problem occurs

when the thickness of the plate is thin, and the distance between the adjacent edges is too close to apply the high frequency approximation. Accordingly GTD would fail to predict the edge diffraction except for the infinitely thin or pretty thick cases [30, 32].

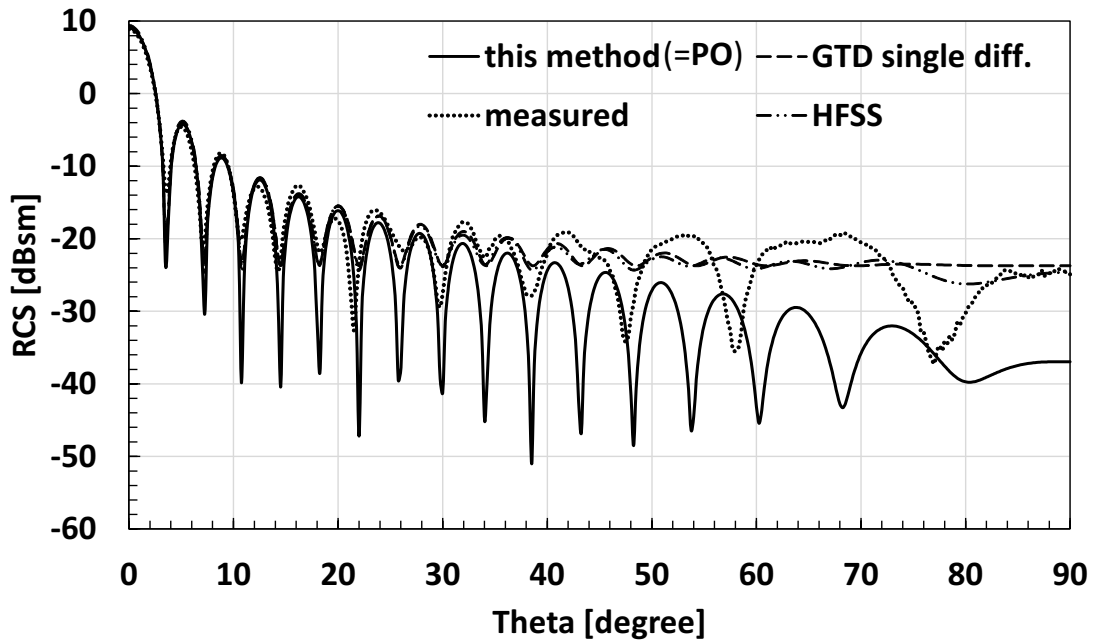
Figure 3.2(b) shows the monostatic RCS of the thin conducting plate S1. Comparisons are made by our proposed method, GTD, the HFSS simulation and measurement in an anechoic chamber at 24 GHz. For the GTD calculation, multiple edge interaction is ignored since the plate size is pretty large ($2a = 2b = 8\lambda$) and the plate thickness ($2c = 0.04\lambda$) was assumed to be infinitely thin. At the specular reflection direction $\theta = 0^\circ$, all the results provide the same peak RCS value of about 9 dBsm. From the specular reflection direction up to $\theta = 50^\circ$, our proposed method explains well the measured data. Figure 3.2(b) shows the effect of the plate thickness for our method. Even though the thickness is very thin (0.04λ), the result with the contribution from the side surface is far better than that of the infinitely thin case at the grazing incidence angles. In the next example, Fig. 3.3 shows the corresponding results for sample S2, which has a finite thickness (0.656λ). Although there are certain differences in terms of the RCS amplitude, especially around $\theta = 45^\circ$, the oscillation behaviors of the proposed method and other results are almost the same.

The third example of the monostatic RCS calculation is given for the rectangular PEC cube S3 ($2a \simeq 2b \simeq 2c \simeq 8\lambda$) in Fig. 3.4. In this case, the proposed method manifests an excellent explanation of the measured monostatic RCS. Not only the locations of local maxima and minima provided by the two results are closer than in the previous cases, the levels of RCS are in close agreement in all direction.

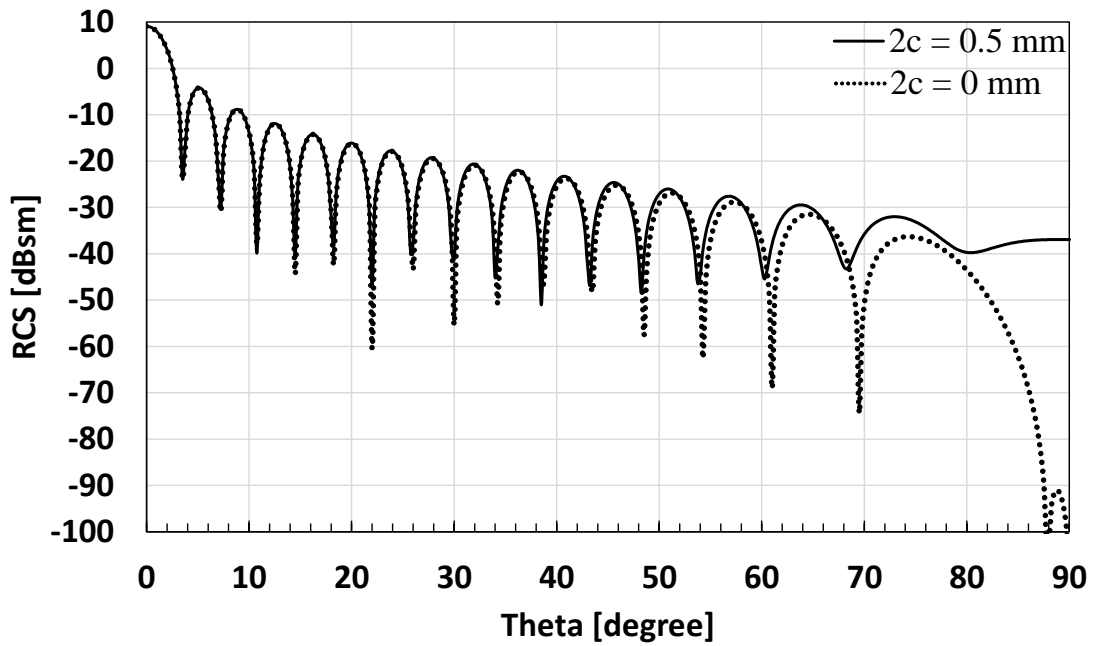
Through the above three examples, one may come to a conclusion that the proposed method can explain accurately the backscattering phenomena of large rectangular PEC cuboids, which are illuminated by TE polarized plane wave.

The bistatic RCS of samples S1, S2, S3 are calculated and compared to those by PO and the HFSS simulations in Figs. 3.5, 3.6, 3.7. Here, TE polarized plane wave illumination is made at 24 GHz from the direction ($\phi_0 = 90^\circ, \theta_0 = 45^\circ$). For these

bistatic RCS calculations, our formulation differs from the conventional PO one, but both results behave almost the same. Three curves have the same peak value (6.06 dBsm) at the specular reflection direction ($\theta = 45^\circ$), and agree well as the thickness of the cuboid gets thicker.



(a)



(b)

Figure 3.2: Monostatic RCS of thin conducting plate S1 ($\phi = \phi_0 = 90^\circ$). (a) —: this method (=PO); - - -: GTD single diff.; - · - · -: HFSS; ·····: measured (b) Thickness consideration —: $2c = 0.5$ mm; ·····: $2c = 0$ mm

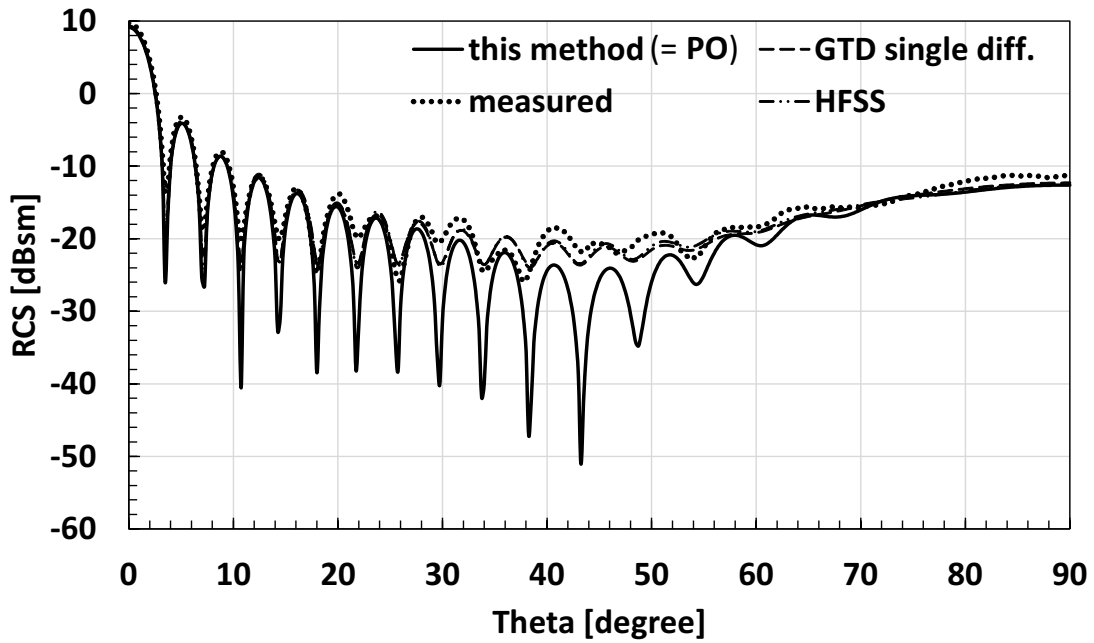


Figure 3.3: Monostatic RCS of conducting cuboid S2 ($\phi = \phi_0 = 90^\circ$).

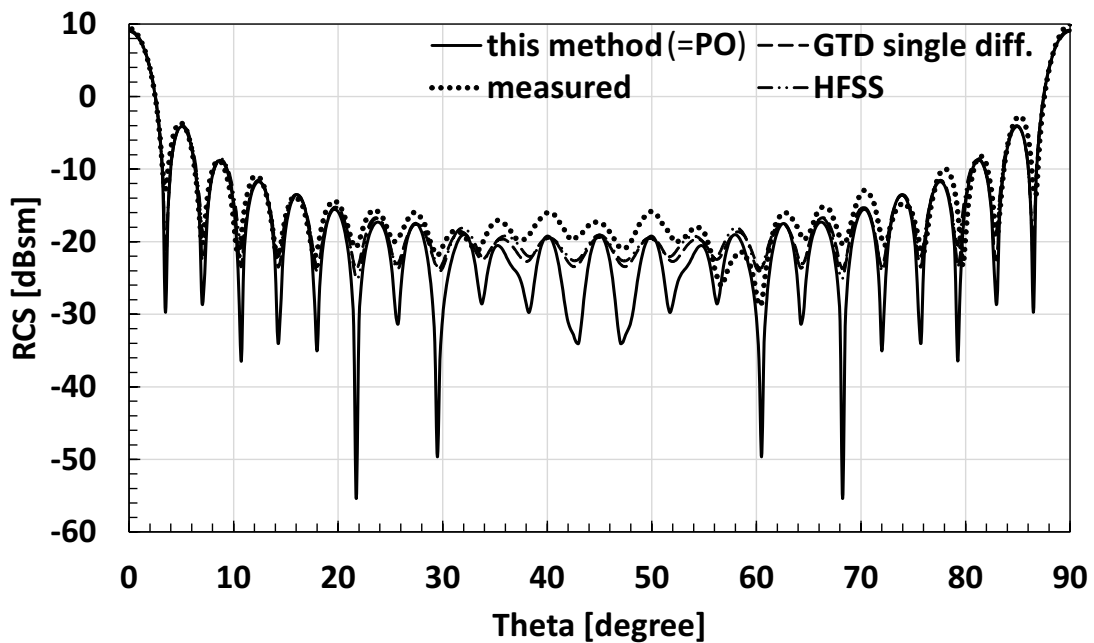


Figure 3.4: Monostatic RCS of aluminum cube S3 ($\phi = \phi_0 = 90^\circ$).

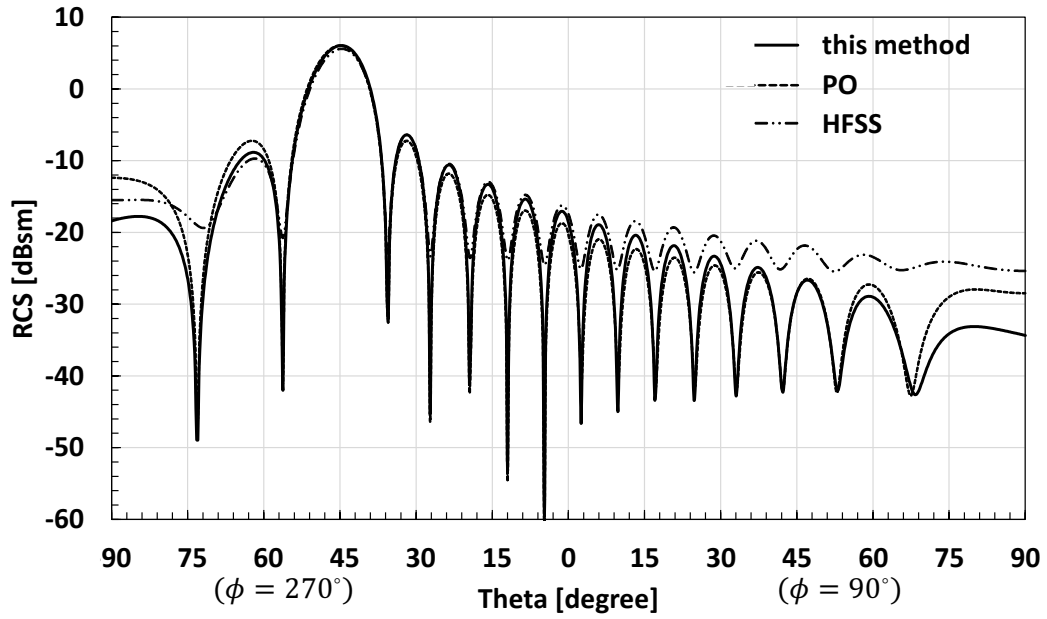


Figure 3.5: Bistatic RCS of thin aluminum plate S1 ($\phi_0 = 90^\circ, \theta_0 = 45^\circ$).

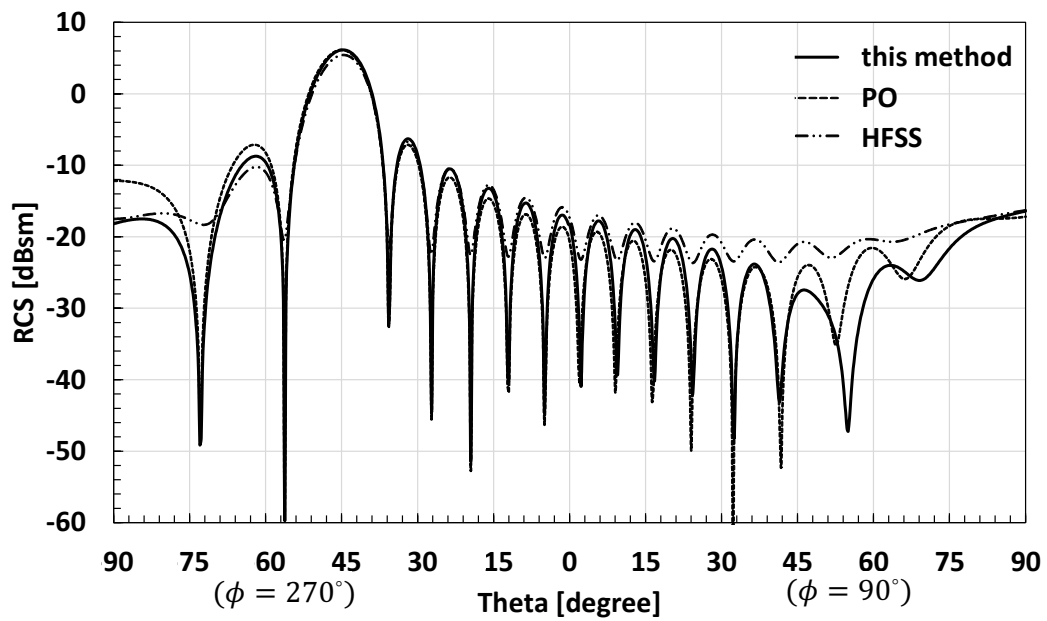


Figure 3.6: Bistatic RCS of aluminum cuboid S2 ($\phi_0 = 90^\circ, \theta_0 = 45^\circ$).

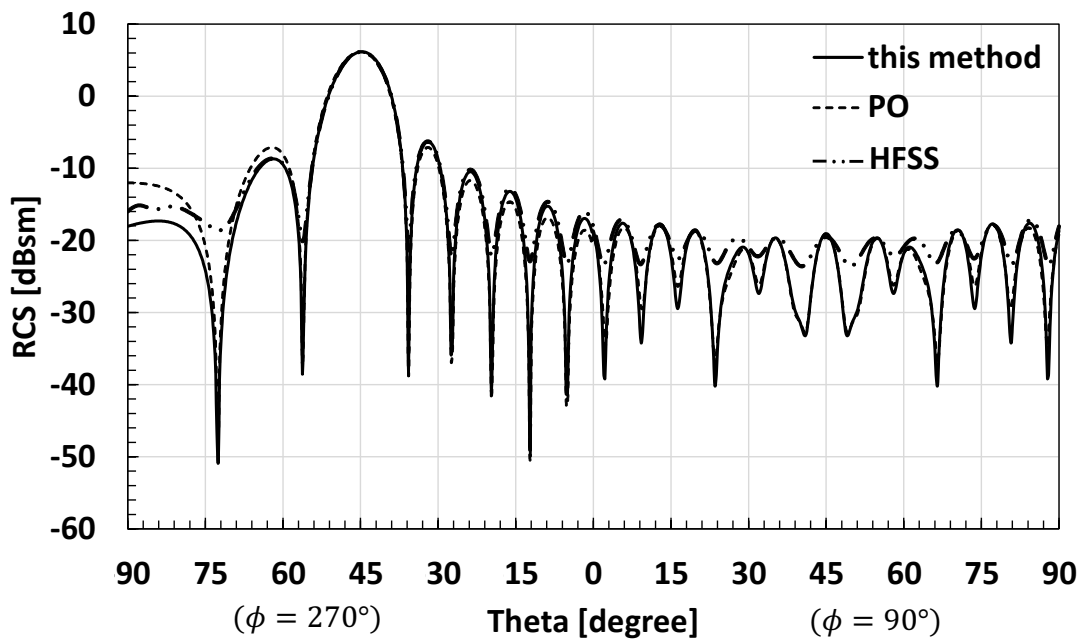


Figure 3.7: Bistatic RCS of aluminum cube S3 ($\phi_0 = 90^\circ, \theta_0 = 45^\circ$).

3.4 Scattering from rectangular dielectric cuboids

Electromagnetic scattering from dielectric bodies is more complex since the incident wave penetrates into the scattering body and excites internal reflected and transmitted waves therein. While the conventional PO and GTD methods cannot be applied for non-PEC bodies, our method can be applied even for dielectric bodies. In this dielectric case, one needs to consider the finiteness of the scattering body to estimate the multiple bouncing effect accurately. Figure 3.8 shows my ray tracing technique to deal with this problem. Figure 3.8 illustrates a typical layout of multiple internal bouncing for $\phi_0 = 90^\circ$. When the incident plane wave impinges on the top surface of a dielectric cuboid, specular reflection $\Gamma_s(\theta_0)$ occurs at the entire top surface S_0 where the equivalent currents \mathbf{J}_0 , \mathbf{M}_0 will be excited. As the internal reflection ($\bar{\Gamma}(\theta') = -\Gamma_s(\theta_0)$) and transmission ($\bar{T}(\theta') = 1 + \bar{\Gamma}(\theta')$) continue, the range S_n of the finally departing rays r_n , on which the additional equivalent currents \mathbf{J}_n , \mathbf{M}_n flow, gets reduced with lateral phase shift, except for the normal

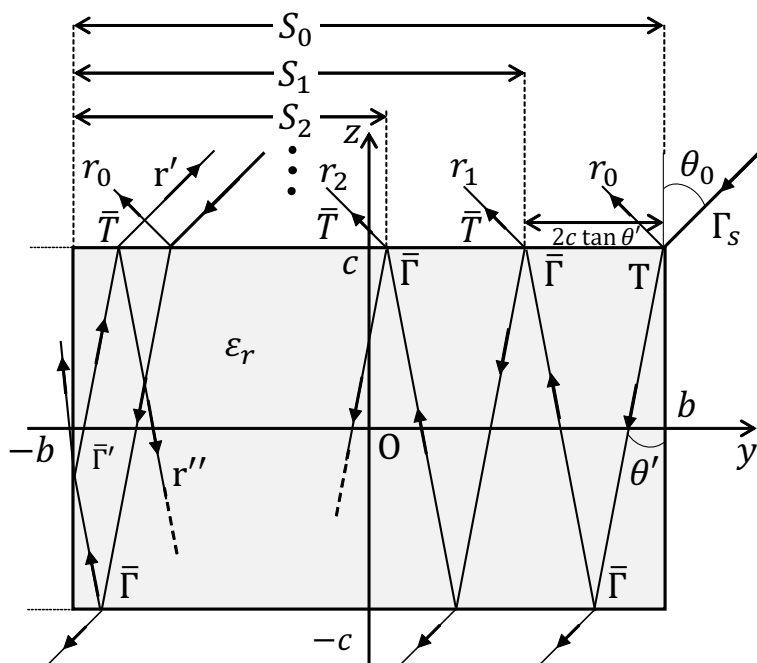


Figure 3.8: Range S_n of the departing rays r_n after n-time internal reflection in yOz plane.

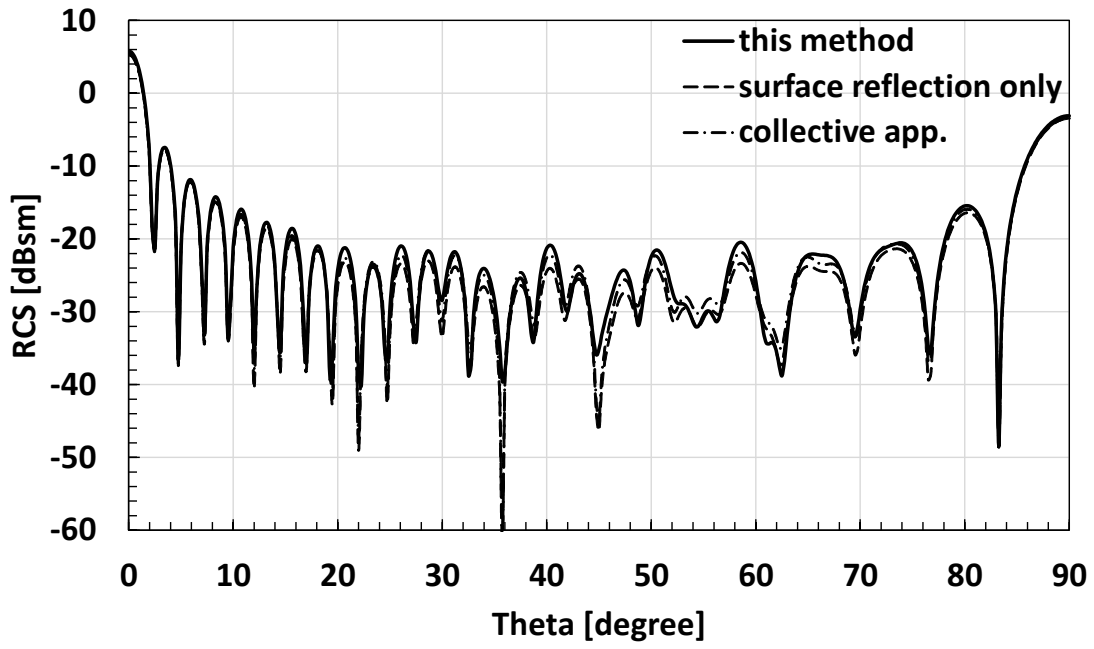
incidence ($\theta_0 = 0^\circ$). Because of the finite dimension $2b$, one may also notice that the internal bouncing rays eventually experience the reflection at the side interface at $y = -b$, and emit two other groups of waves as classified as r' and r'' in Fig. 3.8. This bouncing process continues until all the incident energy dissipates or leaks out. The scattered field formulation due to the above internal bouncing wave is similar to Eqs. (3.10), (3.11), but with a different integration range S_n . In this paper, the contributions of the multiply reflected ray r'' are neglected.

Figures 3.9 ~ 3.11 show the monostatic RCS of dielectric cuboids S4 ~ S6 listed in Table I. Our calculated results are compared with those by the surface reflection only (Eqs. (3.10), (3.11)), by the collective approximation (Eq. (4.3)), by our measurement, and by the HFSS simulation. For these calculations, 5 internal bouncing contributions are sufficient to get a converging result. In addition, the contribution of a transmission from the facet at $y = -b$ in Fig. 3.8 is omitted due to its negligible effect in this monostatic setting.

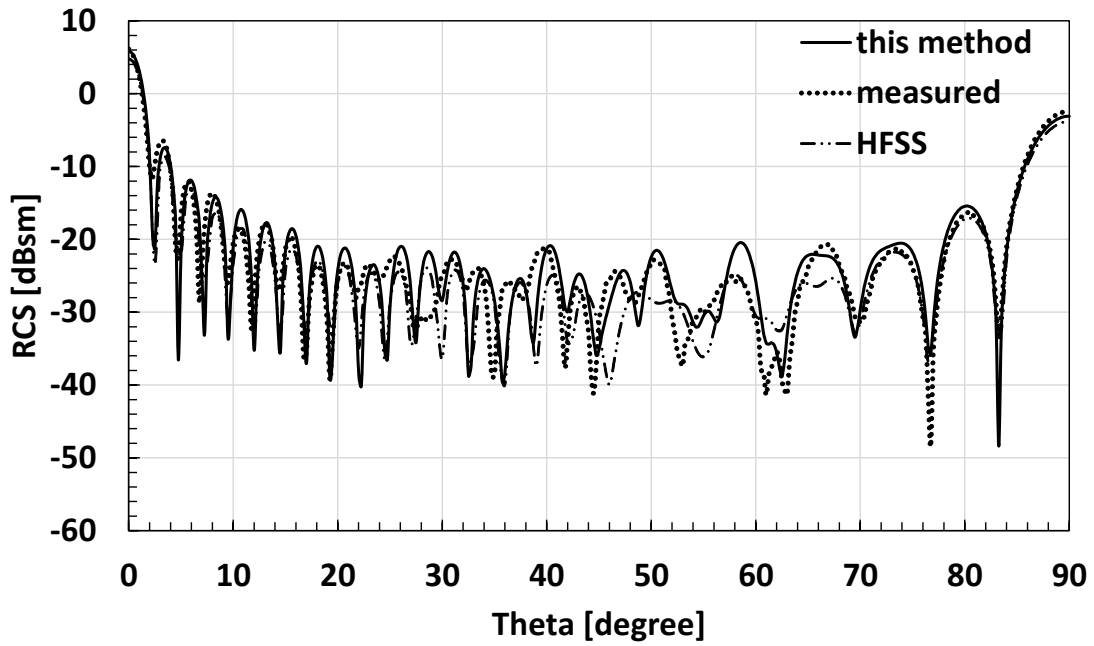
It is found that the main RCS peak due to the specular reflection is predicted correctly by all methods. While three approximation results in Fig. 3.9 (a), which is the most lossy case among three sample materials S4, S5, S6, exhibit almost the same behavior, they become different when the thickness of the cuboid gets thinner, or the material loss gets smaller. Because of the material loss, the effect of multiple bouncing is weak. Accordingly, the surface reflection is dominant and the RCS return is pretty weak (about -20 dBsm) except for the specular reflection direction $\theta = 0^\circ$. Figure 3.10 shows the results for a thinner and smaller loss polymer cuboid S5. One observes an internal bouncing effect even at specular reflection direction, and a strong interaction yields the RCS oscillation for other directions. Final example is shown in Fig. 3.11 for almost loss-less polymer cube S6. Symmetric RCS pattern with respect to angle $\theta = 45^\circ$ should be observed when width $2b$ and thickness $2c$ become exactly the same. However the only difference $2c - 2b = 0.2$ mm in sample S6 makes a slight non-symmetric low RCS pattern around $\theta = 15^\circ$ and 75° . Our result shows a good agreement with our measured data and the HFSS simulated

result, except for the above mentioned low RCS angles. This may be due to the omission of the contributions from the multiply bouncing ray r'' in Fig. 3.8.

Besides, since material S6 has a relatively small dielectric loss, the multiple bouncing effect could be strong causing the difference between the results by the proposed method and the case with only the surface reflection as can be seen in at $\theta = 0^\circ$ and 90° in Fig. 3.11(a). At these two angles, the effect of ray r' also vanishes, therefore the proposed method and the collective approximation model are the same.

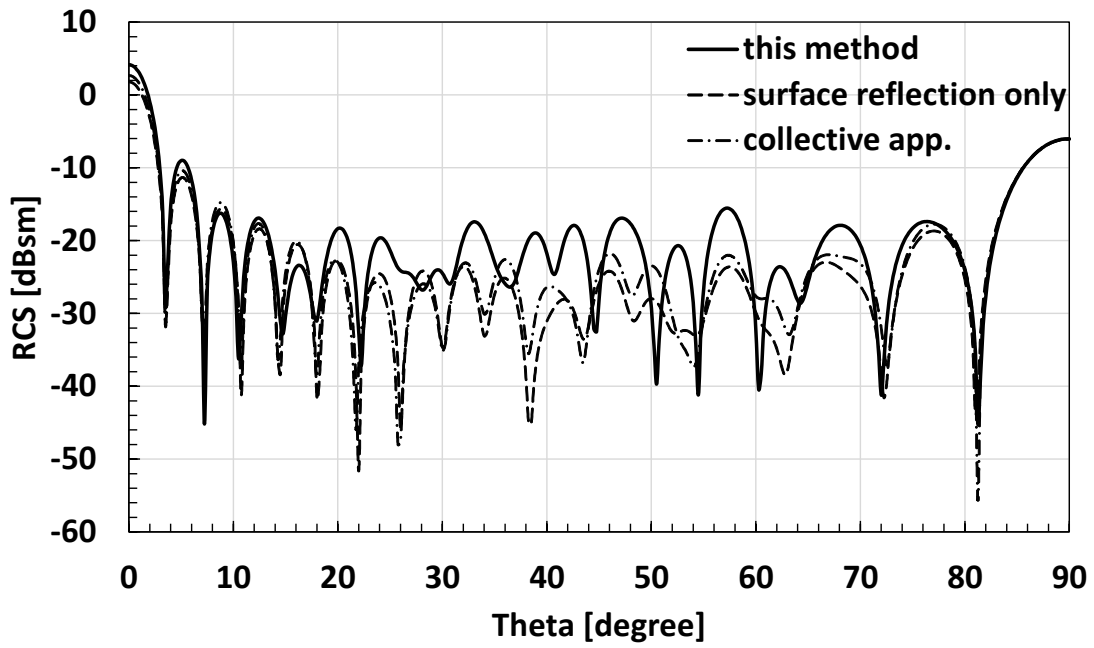


(a)

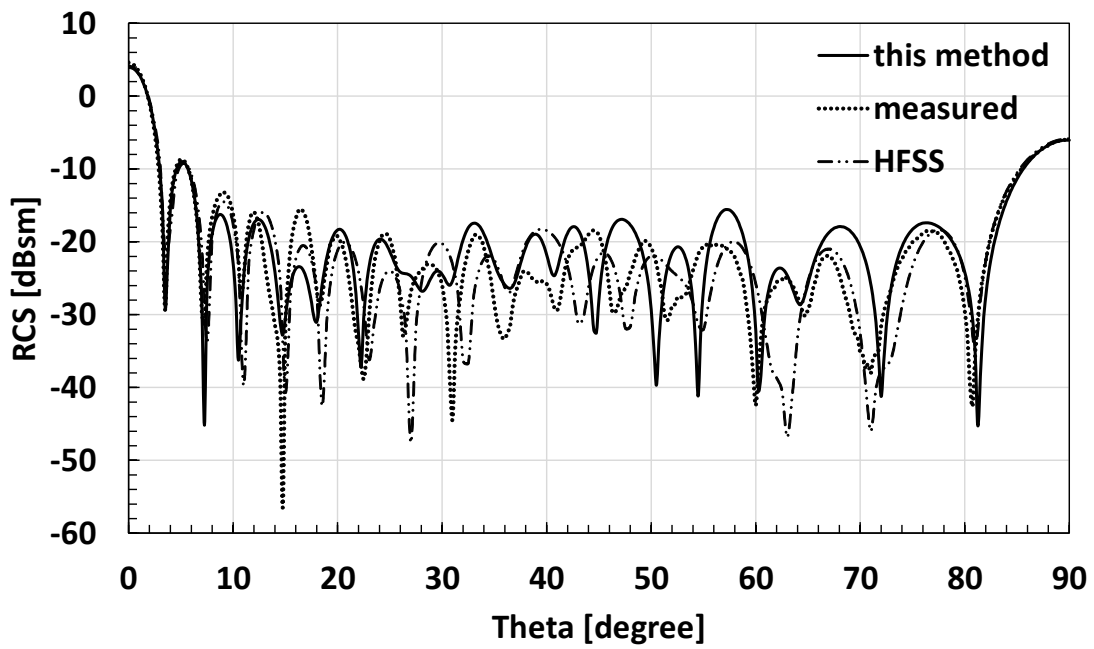


(b)

Figure 3.9: Monostatic RCS of the polymer cuboid S4 ($\phi = \phi_0 = 90^\circ$, 24 GHz). (a) —: this method; ---: surface reflection only; -·-·: collective approximation. (b) —: this method; ····: measured; -·-·-·: HFSS.



(a)

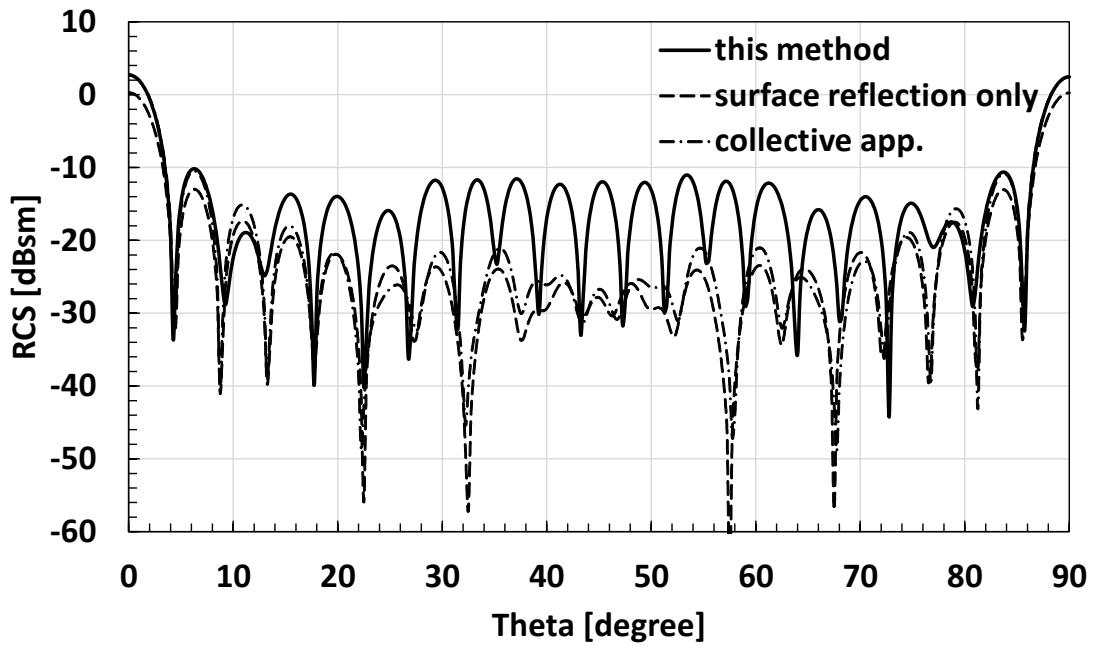


(b)

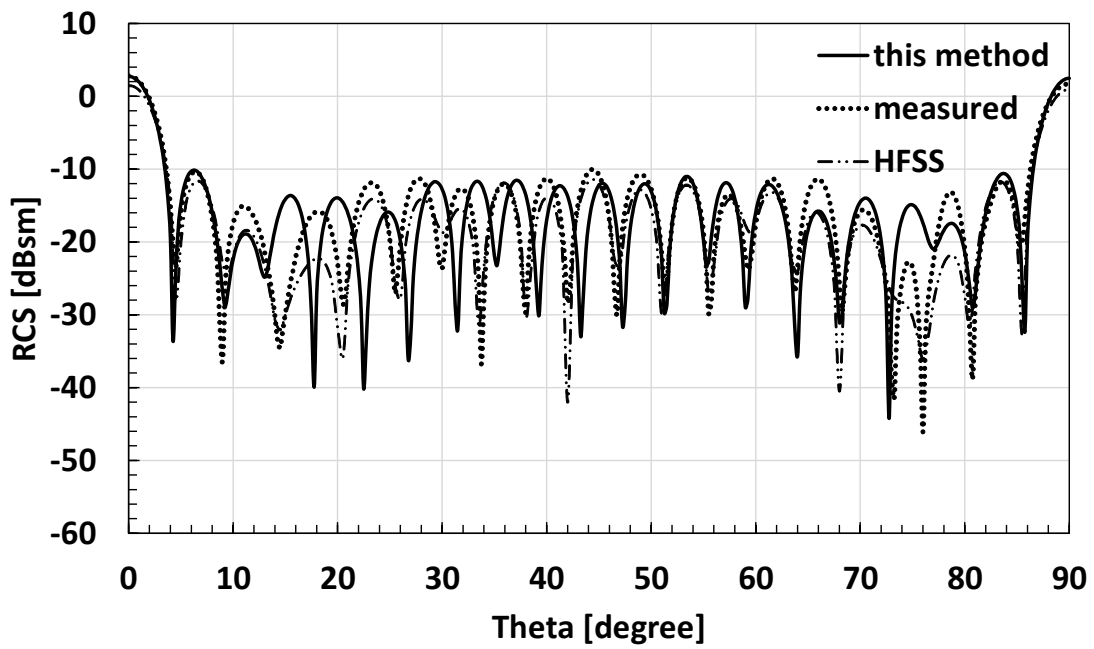
Figure 3.10: Monostatic RCS of the polymer material S5 ($\phi = \phi_0 = 90^\circ$, 24 GHz).

(a) —: this method; ---: surface reflection only; -·-: collective approximation.

(b) —: this method; ·····: measured; -·-·-·-: HFSS.



(a)



(b)

Figure 3.11: Monostatic RCS of the polymer material S6 ($\phi = \phi_0 = 90^\circ$, 19.5 GHz).

(a) —: this method; ---: surface reflection only; -·-·: collective approximation.

(b) —: this method; ·····: measured; -·-·-·: HFSS.

3.5 Conclusions

A new high frequency approximation method to analyze the electromagnetic scattering from rectangular dielectric cuboids has been proposed. The method is based on the assumption that scattering far field is generated by the assumed equivalent electric and magnetic currents excited by the outgoing reflected wave from the scatterer.

From our numerical examples and comparisons, one may conclude that the proposed method is capable of analyzing the scattering phenomena of a rectangular cuboid, either PEC or dielectric, for the TE polarized plane wave illumination. For the latter case, it has been proven that the proposed method gives a better result as one includes the current contribution from the multiple internal bouncing effect. This method may be applicable for the scattering estimation from dielectric polyhedrons or more general edged objects.

The scattering far field of a dielectric cuboid has been estimated by an analytic relation between known information such as frequency, object dimensions and material properties. Such analytic relation and accuracy may provide us with a basis to deal with the inverse problem solving for the material properties when the scattering far field is known. That is the topic to be discussed in the next chapter.

Chapter 4

Dielectric permittivity estimation for solid materials using free space method

In the previous chapter, we have seen that the Kirchhoff approximation provides us with a high frequency approximation method to calculate the monostatic scattering far field of a dielectric cuboid. It has been shown that the method has acceptable accuracy in the normal specular reflection direction. The complex scattering far field can be calculated analytically from known parameters, such as frequency, object dimensions and material properties. That also leads to the possibility to solve the inverse problem to calculate the material properties from the object's measured scattering far field. In order to explain that, this chapter will summarize the relation between the relative dielectric permittivity, the multiple reflection coefficient and the complex far field scattering quantity. Based on this relation, this chapter also will show the systemized steps of our free space method to estimate the relative dielectric permittivity from measured scattering data. Together with the assumptions and conditions, the limit of our method also will be verified. Several examples will be shown to demonstrate the ability of the method.

4.1 The relation between the complex relative dielectric permittivity, the multiple reflection coefficient and the complex scattering quantity

Let's consider the scattering phenomenon from a dielectric cuboid by a TE normal incidence as shown in Fig. 4.1. Chapter 3 has shown a definition of radar cross section (RCS) that relates the scattering quantity to other parameters. Unfortunately, it is not enough to determine the complex value of the multiple reflection coefficient and $\varepsilon_r (= \varepsilon_r' + i\varepsilon_r'')$ because it is a real quantity. However, if one defines a complex scattering quantity $\hat{\sigma}$ as

$$\hat{\sigma} = \lim_{r \rightarrow \infty} 2\sqrt{\pi r} \frac{E_y^s}{E_y^i} e^{-ikr}, \quad (4.1)$$

then the conventional RCS can be given by $|\hat{\sigma}|^2$ from Eq. (4.1). Here, k is the free space wavenumber, and E_y^i and E_y^s denote the incident and the scattered electric field at the observation point with distance r from the origin, respectively, as shown in Fig. 4.1. H_x^r and E_y^r stand for the magnetic and electric fields of the primary surface reflected wave excited without multiple reflections inside the material body, respectively.

When a dielectric cuboid of the length $2a$, the width $2b$, the thickness $2c$ and the relative permittivity ε_r is illuminated by a TE polarized electromagnetic plane wave, one gets from Ref. [33] as

$$\hat{\sigma} = -\frac{4ikab}{\sqrt{\pi}} \Gamma_m e^{-2ikc}, \quad (4.2)$$

with Γ_m is the multiple reflection coefficient from the dielectric cuboid. Γ_m has the general form of Eq. 4.3. However, in the normal reflection direction, it can be simplified by

$$\Gamma_m = \frac{\Gamma_s(1 - e^{i4kc\sqrt{\varepsilon_r}})}{1 - \Gamma_s^2 e^{i4kc\sqrt{\varepsilon_r}}} \quad (4.3)$$

with Γ_s is the surface reflection coefficient calculated from the primary surface reflected field E_y^s at $z = c$:

$$\Gamma_s = \frac{1 - \sqrt{\varepsilon_r}}{1 + \sqrt{\varepsilon_r}}. \quad (4.4)$$

As a brief verification, Fig. 4.2 shows the monostatic RCS values in the frequency domain of a nylon cuboid estimated by our Kirchhoff approximation and obtained by measurement. The relative permittivity ε_r of the nylon cuboid is assumed to be constant, $\varepsilon_r = 3.023 + i0.043$, in the whole frequency range. This ε_r is the average value of those measured by the open-ended probe method, as shown in Table 4.1. As can be seen, the two results have close agreement in most of the frequency range. However, there are deviations at frequencies around 21 and 24 GHz. Since these deviations occur at low RCS values, at which the phase errors of multiply bouncing rays play an important role for the cancellation, these errors may be due to the inaccuracy of the assumed relative permittivity.

Equations (4.2), (4.3), (4.4) show us a clear connection between the complex scattering far field, the reflection coefficient and the relative dielectric permittivity. In the next section, these equations will be utilized to extract the relative dielectric permittivity when the complex scattering far field is known.

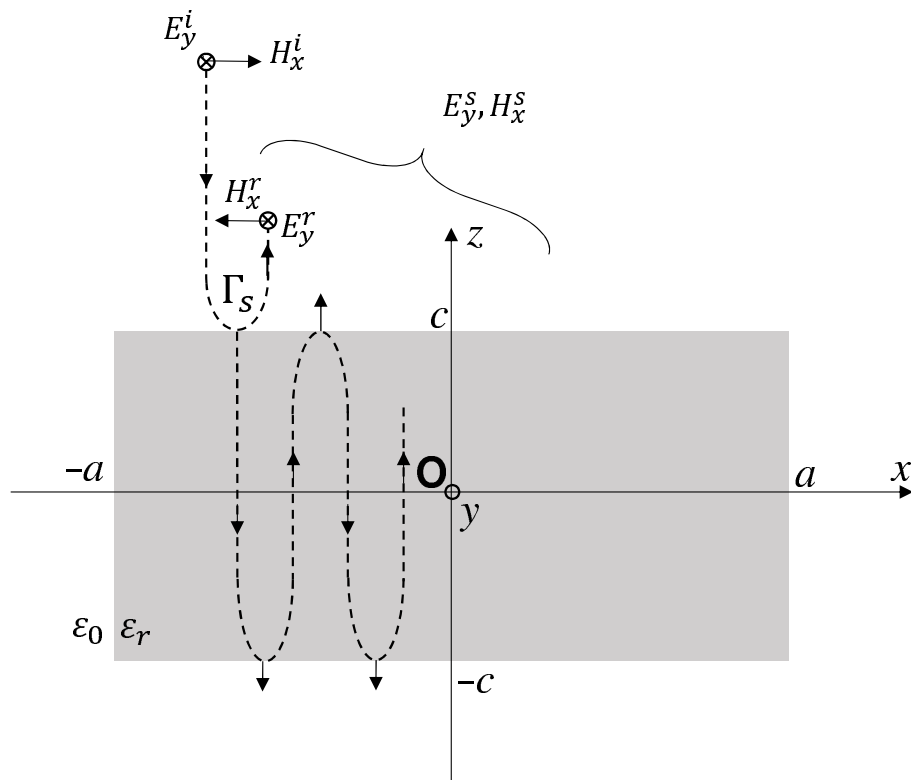


Figure 4.1: TE polarized plane wave scattering from a rectangular dielectric cuboid at the normal incidence.

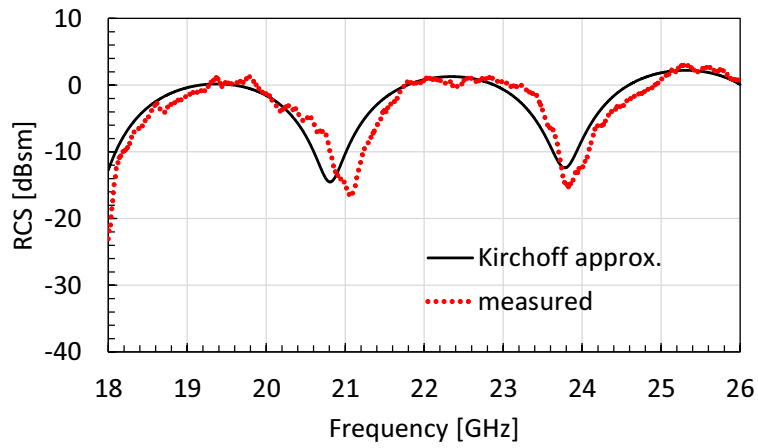


Figure 4.2: Monostatic RCS of a nylon cuboid in the frequency domain ($2a = 2b = 100.0$ mm, $2c = 29.0$ mm). The relative permittivity $\epsilon_r (= 3.023 + i0.043)$ is assumed to be the average value measured by the open-ended coaxial probe method given in Table 4.1.

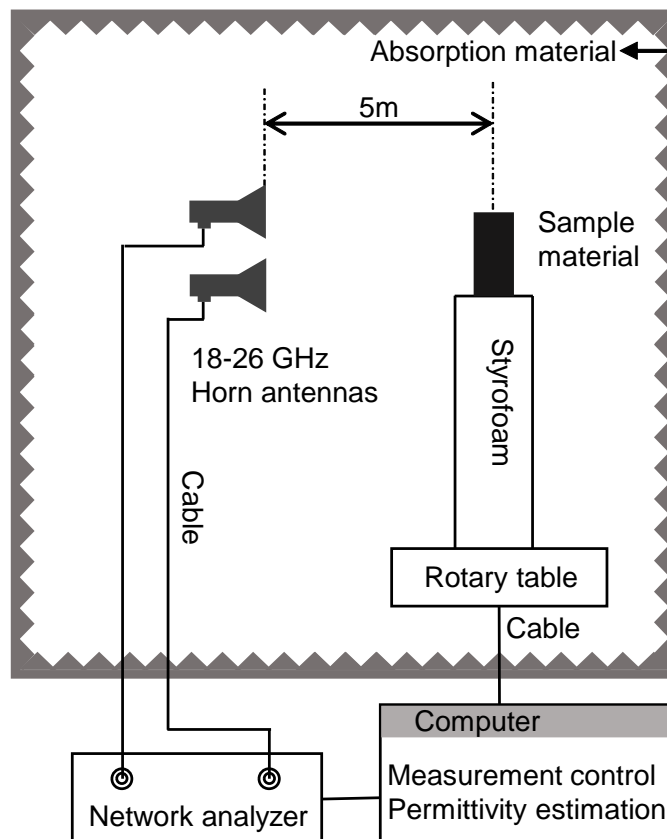


Figure 4.3: Schematic diagram of the measurement configuration.

4.2 Permittivity estimation method

Figure 4.3 is aimed to provide a clearer imagination on the measurement configuration of our free space method. The transmit and receive horn antennas are aligned in parallel in order not to lose the dynamic range of the measurement by an insertion of a directional coupler. A sample material is placed on a Styrofoam pillar in an anechoic chamber, more than 5 m away from the antennas to guarantee the far field condition. The rotary table is used to adjust position so that the antennas are in the normal specular direction of the sample's surface. When the complex scattering quantity $\hat{\sigma}$ is obtained from measurements, the multiple reflection coefficient can be calculated from Eq. (4.2) by

$$\Gamma_m = -\frac{\sqrt{\pi}}{4ikab}\hat{\sigma}e^{2ikc}. \quad (4.5)$$

As can be seen, Γ_m is a multivalued function of ε_r . For a certain value of Γ_m , there are several potential mathematical solutions of ε_r . And it is difficult to obtain the physical relative permittivity by solving Eq. (4.3) analytically. Therefore, an iterative numerical method is used to find the value of ε_r in this work. The convergence of this numerical calculation to the correct value needs to be secured by an appropriate selection of the initial guess of ε_r . For many applications, this means an understanding of the class of materials or the material properties. In this research, we developed an algorithm to calculate the proper initial guess effectively without knowing the relative permittivity range of the material in advance.

The multiple reflection coefficient Γ_m can be interpreted physically by an infinite sum of the successive internal reflected waves as illustrated in Fig. 4.1. This fact is also revealed by the Taylor series of Γ_m as

$$\Gamma_m = \Gamma_s - \Gamma_s(1 - \Gamma_s^2)e^{i4kc\sqrt{\varepsilon_r}} - \Gamma_s^3(1 - \Gamma_s^2)e^{i8kc\sqrt{\varepsilon_r}} - \dots. \quad (4.6)$$

From Eq. (4.6), it is predictable that Γ_m oscillates around and approaches to Γ_s as the cuboid thickness $2c$ goes to infinity, or when the imaginary part of ε_r is large. Since materials under test are assumed to be weakly dispersive and to have a

linear dielectric property in the frequency range of interest, so the surface reflection coefficient Γ_s will be predictably linear. Therefore, with the given assumptions, a linear least squares approximation of Γ_m could be a good estimation of Γ_s . Then, this approximated reflection coefficient $\bar{\Gamma}_s$ can yield a reference relative permittivity $\bar{\epsilon}_r$, located near the true ϵ_r , by solving Eq. (4.4) as

$$\bar{\epsilon}_r = \left(\frac{1 - \bar{\Gamma}_s}{1 + \bar{\Gamma}_s} \right)^2. \quad (4.7)$$

Now one needs to find $\bar{\Gamma}_s$. Given a set of multiple reflection coefficients Γ_m at different frequencies, for example as shown in Fig. 4.4, the following linear approximation scheme is used to obtain $\bar{\Gamma}_s$, provided the material sample is assumed to have a thickness larger than the limit thickness given in Sect. 4.3.

First, identify all the local extrema of the real part of Γ_m . If the numbers of maxima and minima are both less than 2 in a desired measurement frequency range, then Γ_s is almost equal to Γ_m and one can calculate $\bar{\epsilon}_r$ via Eq. (4.7) but replacing $\bar{\Gamma}_s$ with Γ_m . If any one of the numbers of local extrema is larger than 1, one can take a least squares approximation of the multiple reflection coefficient in the interval from the first to the last of the corresponding extrema, as seen in Fig. 4.4. To illustrate how near the approximation can approach the true surface reflection coefficient Γ_s , two ideal examples are given in Figs. 4.5, 4.6. The multiple reflection coefficient of a dielectric slab with fixed thickness was calculated and approximated by the proposed approximation with two known different permittivities. Then, the approximated coefficients were compared with the true surface reflection coefficients Γ_s . Very good agreement was observed in both cases.

In practice, measurements may suffer from a noise interference so that the real part of the reflection coefficient may not be smooth as seen in the ideal case in Fig. 4.4, but have small oscillations as shown in Fig. 4.7, for example. In such situations, one may need to find the true local extrema of Γ_m . This local extrema finding process may be possible by selecting the extrema twice from the measurement data [34]. When the extrema selections are impossible, one can take the normal least squares approximation of Γ_m in the whole frequency range.

Depending on thickness $2c$, the approximations of the multiple reflection coefficient by the proposed approach and by the normal least square approximation may differ significantly. An example using a dielectric cuboid with known relative dielectric permittivity $\varepsilon_r = 3.00 + i0.01$ from 18–26 GHz is shown in Fig. 4.8. In this example, the reflection coefficient approximated using the proposed way quickly converged to the true coefficient. The convergence in the case of approximation using the normal least square approximation was slower.

The same process is applied to get the imaginary part of the approximate surface reflection coefficient $\bar{\Gamma}_s$ from the multiple reflection coefficient Γ_m , and the real and the imaginary parts are combined to get a complex value $\bar{\Gamma}_s$ for $\bar{\varepsilon}_r$.

Based on the assumptions and predictions prescribed above, a method proposed here can be summarized in the followings when the sample's cubic dimensions are given:

- 1) Measure the complex scattering quantity $\hat{\sigma}$ in the specular (normal) reflection direction.
- 2) Extract the multiple reflection coefficient Γ_m from the complex scattering quantity $\hat{\sigma}$ using Eq. (4.5).
- 3) Find a linear least squares approximation $\bar{\Gamma}_s$ of Γ_m .
- 4) Initial reference values of the relative dielectric permittivity $\bar{\varepsilon}_r$ is calculated from $\bar{\Gamma}_s$ via Eq. (4.7).
- 5) Eq. (4.3) is solved iteratively to find a correct value of ε_r .

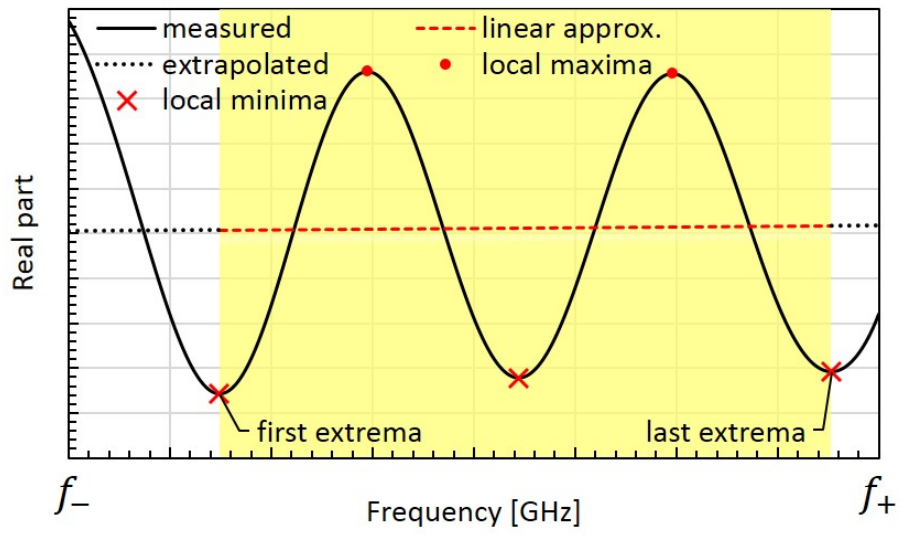


Figure 4.4: Example of least squares approximation of the real part of $\bar{\Gamma}_s$ from the multiple reflection coefficient Γ_m .

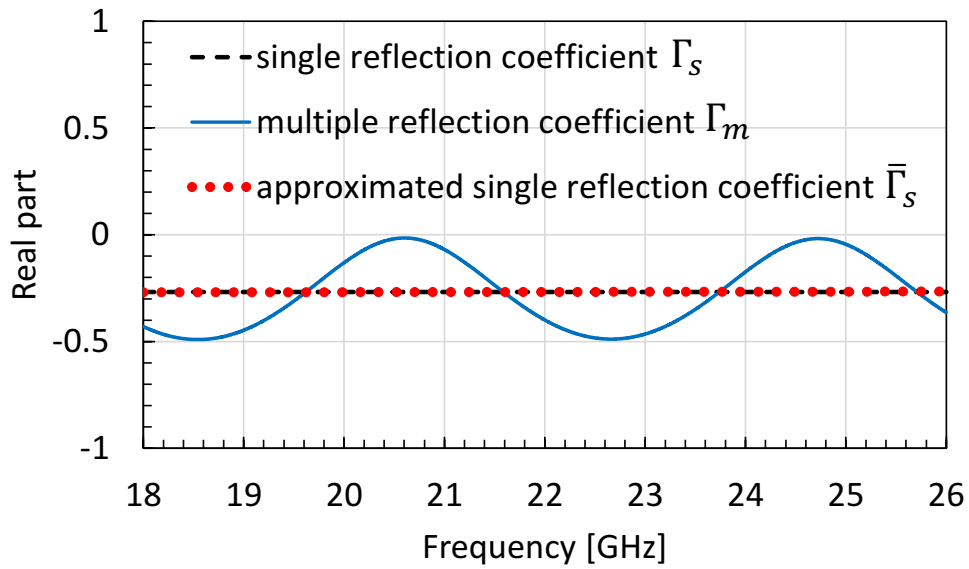


Figure 4.5: Approximation of the real parts of the multiple reflection coefficients of a 21-mm thick dielectric slab, $\epsilon_r = 3.00 + i0.01$.

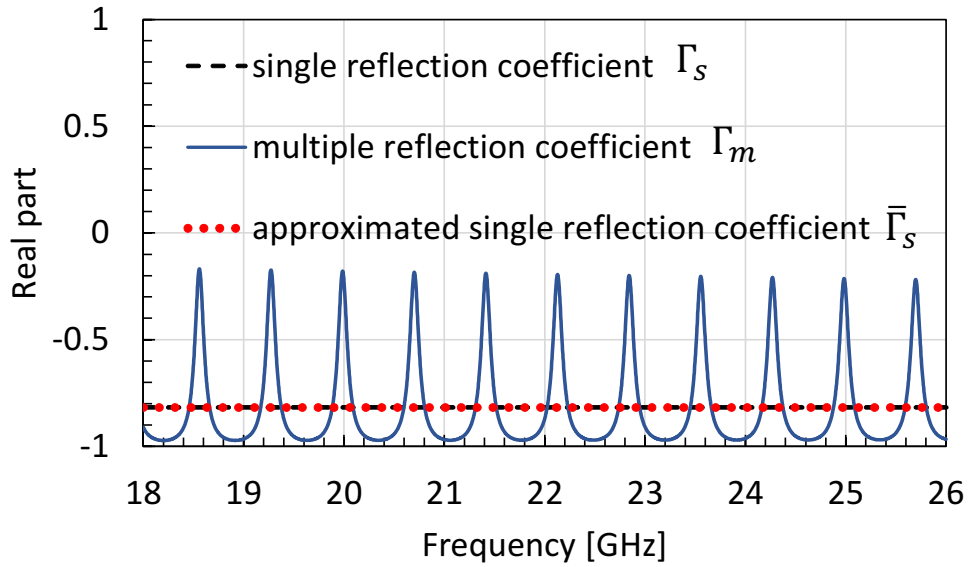


Figure 4.6: Approximation of the real parts of the multiple reflection coefficients of a 21-mm thick dielectric slab, $\epsilon_r = 100.00 + i0.01$.

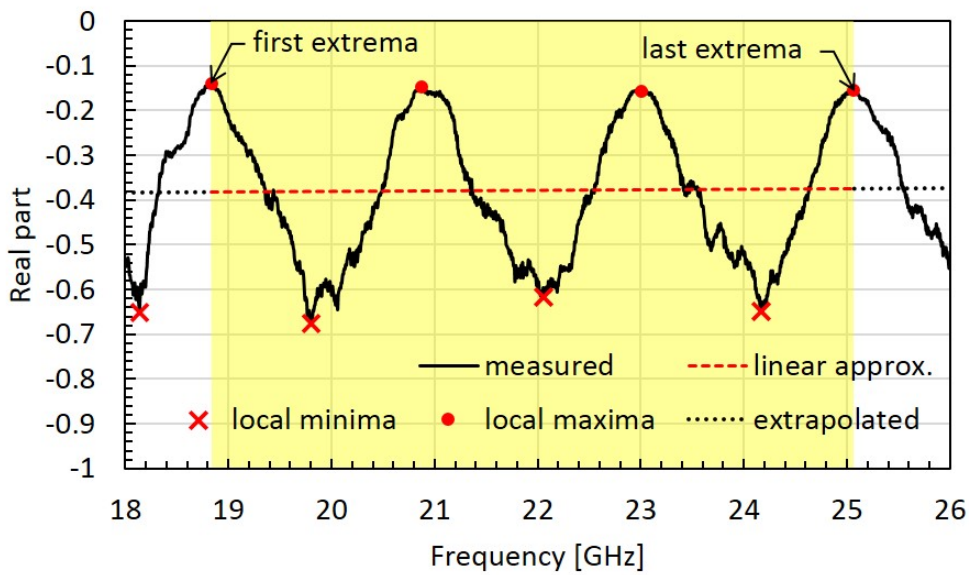


Figure 4.7: Least squares approximation of the real part of $\bar{\Gamma}_s$ from the measured multiple reflection coefficient Γ_m of a Macor cuboid ($2a = 2b = 100.0$ mm, $2c = 30.0$ mm).

4.3 Requirements of the method

Our method is based on the assumptions that the material-under-test is isotropic, homogeneous and non-magnetic. Because a linear least squares approximation of the multiple reflection coefficient is used, the material is assumed to have a weakly dispersive complex relative permittivity. Regarding dimensions, a sample needs to be finely machined to cuboid shape. With the use of the Kirchhoff approximation in the scattering solution, the sample's surface of the measurement is required to be electrically large comparing to the measuring wavelength.

The observations and the analyses on Eq. (4.3) reveal that when the dielectric sample is very thick or possesses a high dielectric constant, the linear approximation $\bar{\Gamma}_s$ will closely resemble Γ_s since these conditions ensure a sufficient number of the oscillation of Γ_m in the measured frequency range. In such a situation, our estimation scheme works well. However, there are cases when there are less than two extrema in oscillation. The first case is when the dielectric sample has almost an infinite thickness or highly lossy property. In this situation, the Γ_m function itself closely approaches Γ_s , resulting in a desirable estimation. The other case is when the sample thickness is thin and the relative dielectric constant is low. When the sample thickness is sufficiently thin, our approach may become inapplicable since the linear approximation of Γ_m may not be in the desirable vicinity of the true Γ_s . The minimal thickness, to which our method can be applied, may be found by analyzing the oscillation of Γ_m as a function of frequency, the sample's thickness and relative dielectric permittivity for the number of its extrema in the measurement frequency range ($f_- \leq f \leq f_+$). One can find the minimal applicable thickness of the sample as

$$2c_{min} = \frac{(M + 2)v_0}{4f_+ \text{Re} \left[\sqrt{\langle \varepsilon_r \rangle} \right]}, \quad (4.8)$$

$$M = \text{Int} \left[\frac{2f_-}{f_+ - f_-} \right] + 1, \quad (4.9)$$

where v_0 is the speed of light in free space, $\langle \varepsilon_r \rangle$ is the average relative permittivity

value in the measurement range and $\text{Int} [\chi]$ denotes the integer part of χ .

Let us discuss on the minimal thickness of samples to assure the validity of our estimation method. A special attention is needed for the case when $|\varepsilon_r| \sim 1$.

From Eq. (4.6), one may notice that the first interaction from the bottom surface arises from the second term $\Gamma_s(1 - \Gamma_s^2)e^{i4kc\sqrt{\varepsilon_r}}$. Thus the real and imaginary parts of Γ_m oscillate due to the phase term $4kc\sqrt{\varepsilon_r}$. In order to secure a stable approximation $\bar{\Gamma}_s$ for Γ_m , one needs at least two consecutive maxima or minima in a measurement frequency range from f_- to f_+ . For frequencies f_1, f_2 ($0 < f_- \leq f_1 < f_2 \leq f_+$), the above requirement can be written with a positive integer m as

$$\frac{8\pi f_1 c \text{Re} [\sqrt{\varepsilon_r}]}{v_0} = m\pi, \quad (4.10)$$

$$\frac{8\pi f_2 c \text{Re} [\sqrt{\varepsilon_r}]}{v_0} = (m + 2)\pi, \quad (4.11)$$

where v_0 is the speed of light in free space and $\text{Re} [\chi]$ denotes the real part of χ .

If the material is weakly dispersive on the measurement range, one may use the measured average value $\langle \varepsilon_r \rangle$ for ε_r . Then taking the ratio f_1/f_2 from Eqs. (4.10) and (4.11), one gets

$$\frac{f_1}{f_2} = \frac{m}{m + 2} \geq \frac{f_-}{f_+} = R, \quad (4.12)$$

and the minimal integer M can be found from this inequality as

$$M = \text{Int} \left[\frac{2R}{1 - R} \right] + 1 = \text{Int} \left[\frac{2f_-}{f_+ - f_-} \right] + 1, \quad (4.13)$$

where $\text{Int} [\chi]$ denotes the integer part of χ . Accordingly, the minimal thickness $2c_{min}$ of the sample material can be derived from Eq. (4.11) as

$$2c_{min} = \frac{(M + 2)v_0}{4f_+ \text{Re} [\sqrt{\langle \varepsilon_r \rangle}]} < 2c = \frac{(m + 2)v_0}{4f \text{Re} [\sqrt{\langle \varepsilon_r \rangle}]} \quad (4.14)$$

As one clearly sees from the above condition, the minimum thickness $2c_{min}$ is related with the sample's relative permittivity ε_r and the measurement range. For totally unknown materials, one may assume $\langle \varepsilon_r \rangle = 1$ as an initial guess. For our present examples, the measurement frequency range is set as 18–26 GHz due to the usage

range of the horn antenna. Then $2c_{min}$ becomes 11.6 mm, 12.6 mm and 8.5 mm for nylon, acrylic and Macor ceramic, respectively. These values are feasible sample sizes for practical measurements.

Given two samples materials, namely nylon and colored acrylic, which have the relative dielectric permittivity approximately as $\epsilon_r = 3.00 + i0.01$, the possibility of estimation was verified at several thicknesses. The successful and unsuccessful estimations at different sample thicknesses were shown in Fig. 4.9 in accordance with the amount of difference shown in Fig. 4.8. Due to lack of proper thickness, estimation at 11.6 mm was not conducted. However, Fig. 4.9 shows successful estimation down to 12 mm. This may be considered as an evidence to confirm the theoretical thickness limit described above.

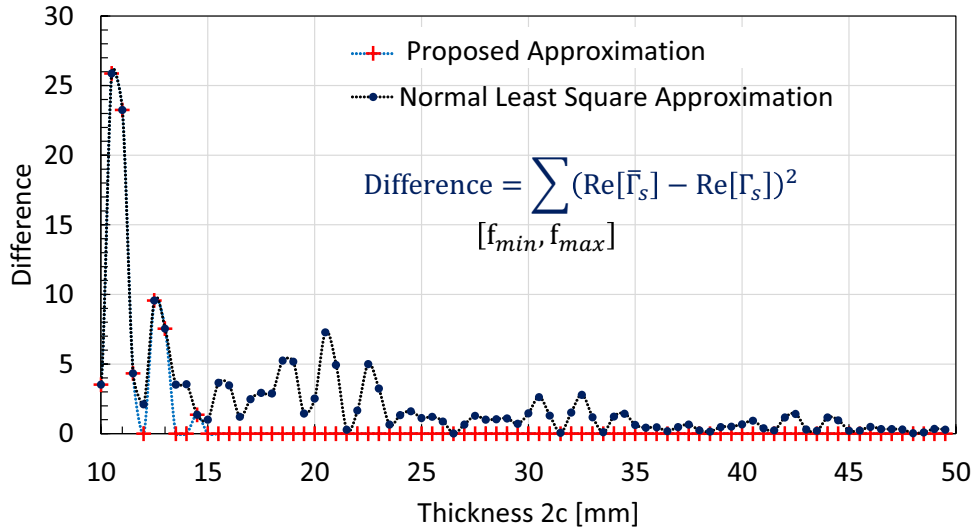


Figure 4.8: An example of the differences between the approximated reflection coefficients and the true surface reflection coefficient.

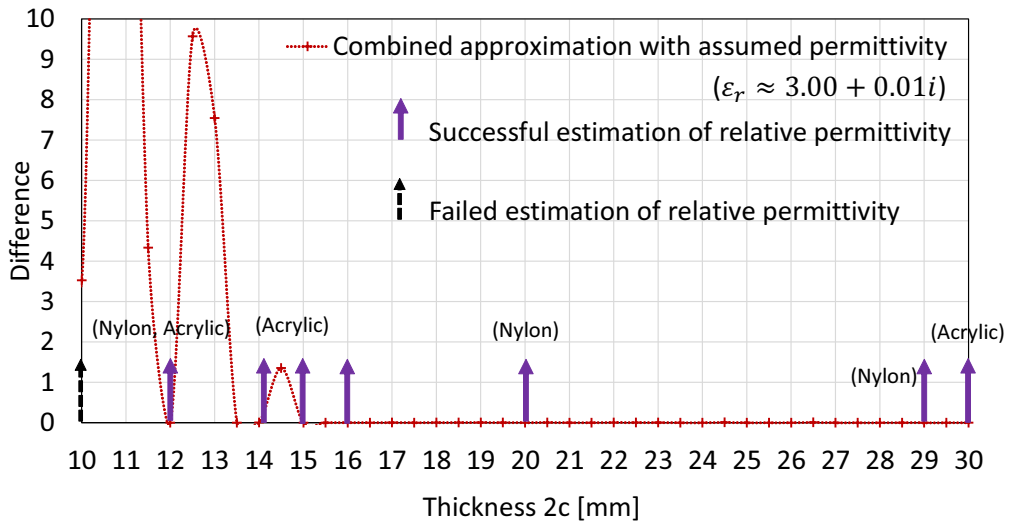


Figure 4.9: Relative permittivity estimations at different thicknesses of nylon and colored acrylic slabs.

4.4 Measurements and discussions

Relative permittivities of several material samples were estimated to verify the validity of our method. The samples are machine-milled with accuracy of ± 0.1 mm and dimensions as described in Table 4.1. Estimations were performed following the scheme proposed in Sect. 4.2. The results were then compared with those obtained by a commercial open-ended coaxial probe method provided by the Agilent Technology. The frequency range (18–26 GHz) is selected due to the usage range of the horn antennas for our RCS measurements.

Our method and the open-ended coaxial probe method have agreed well on the permittivities for nylon and acrylic samples throughout the frequency range as can be seen in Figs. 4.10 and 4.11. Estimations by both methods show that nylon and acrylic have relatively low loss with the respective imaginary parts ε_r'' oscillating around 0.042 and 0.035, while the real parts ε_r' of the two relative permittivities are relatively constants varying around 3.00 and 2.57. Since the open-ended coaxial probe method is a well studied and confirmed method, these agreements verified the validity of estimations by my method.

Figure 4.12 shows results of Macor ceramic's relative permittivity by our method, the open-ended probe method and reference values at 19.0 and 20.0 GHz in Ref. [35]. At two frequencies given above, our method and the reference have close estimations. This again confirmed the validity of my estimation. Regarding the result by the open-ended probe method, while the estimated real part ε_r' by the open-ended probe method is close to the values by our method, the measured imaginary part ε_r'' is not reliable, because these values are negative. This may be due to the improper contact of the probe caused by a surface irregularity of the sample, or by a calibration error of the short measurement. This case of Macor ceramic sample is an example illustrating the difficulties of the open-ended coaxial probe method in dealing with solid samples. Meanwhile, my method works fine.

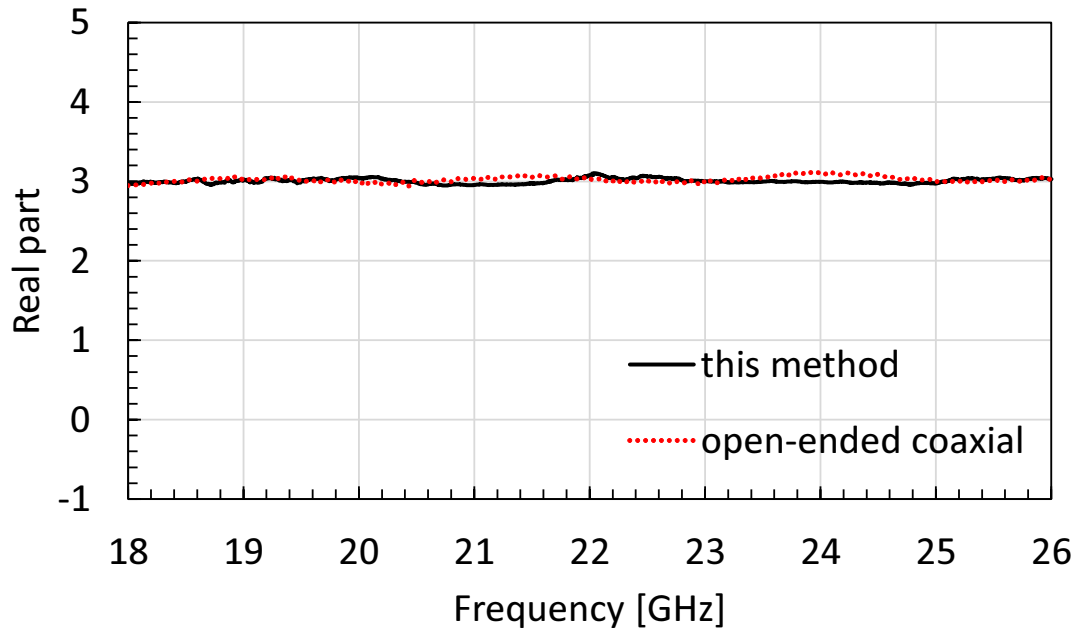
In order to estimate the relative permittivity of the material under test without knowing the relative permittivity range of the material in advance, the assumptions

Table 4.1: Sample materials and their relative permittivities

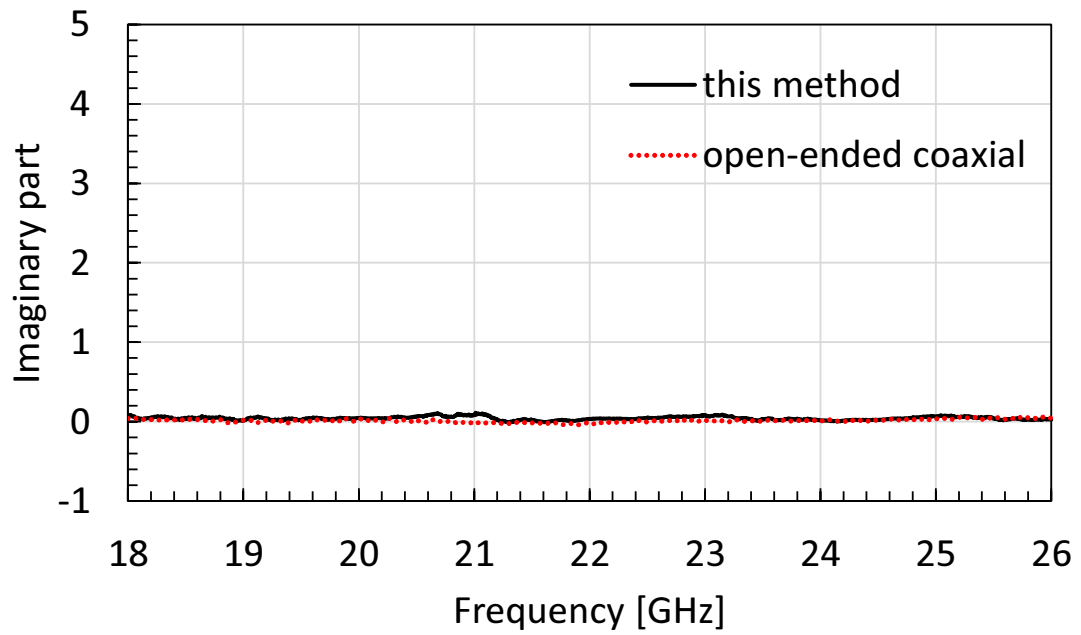
Material	$2a$ [mm]	$2b$ [mm]	$2c$ [mm]	Open-ended coaxial $(\langle \varepsilon_r' \rangle, \langle \varepsilon_r'' \rangle)$	Our result $(\langle \varepsilon_r' \rangle \pm \sigma', \langle \varepsilon_r'' \rangle \pm \sigma'')$
Nylon Type 6	100.0	100.0	29.0	(3.023, 0.043)	$(3.004 \pm 0.031, 0.042 \pm 0.021)$
Cast acrylic	100.0	100.0	30.0	(2.625, 0.037)	$(2.578 \pm 0.017, 0.035 \pm 0.021)$
Macor ceramic	100.0	100.0	30.0	(5.678, -0.433)	$(5.673 \pm 0.028, 0.070 \pm 0.021)$

mentioned in Sect. 4.3 are necessary. With these assumptions, the physical Γ_s will behave like a linear function and can be approximated quite accurately from the oscillating Γ_m as explained in the second paragraph of Sect. 4.2. As a result, the initial guesses for the estimation process will be located close to the physical value of relative permittivity, hence a fast convergence is secured. In the experimented cases, estimation converges after several steps for 5-digit accuracy.

Percent cumulative probability distributions of the permittivities of three samples around the respective average values are given in Figs. 4.13, 4.14, 4.15, 4.16, 4.17, 4.18. As can be seen, our measurement values obey Gaussian distribution. Accordingly, the true value would be located within the average value $(\langle \varepsilon_r' \rangle + i\langle \varepsilon_r'' \rangle)$ plus minus one standard deviation $\sigma' \pm i\sigma''$. These results are summarized in Table 4.1. Given that a dielectric measurement by a typical open-ended coaxial probe normally has an accuracy of 5% of $|\varepsilon_r|$ for both real and imaginary parts [36], it may be concluded that our method has a more stable estimation of the relative permittivity than the open-ended coaxial probe method.

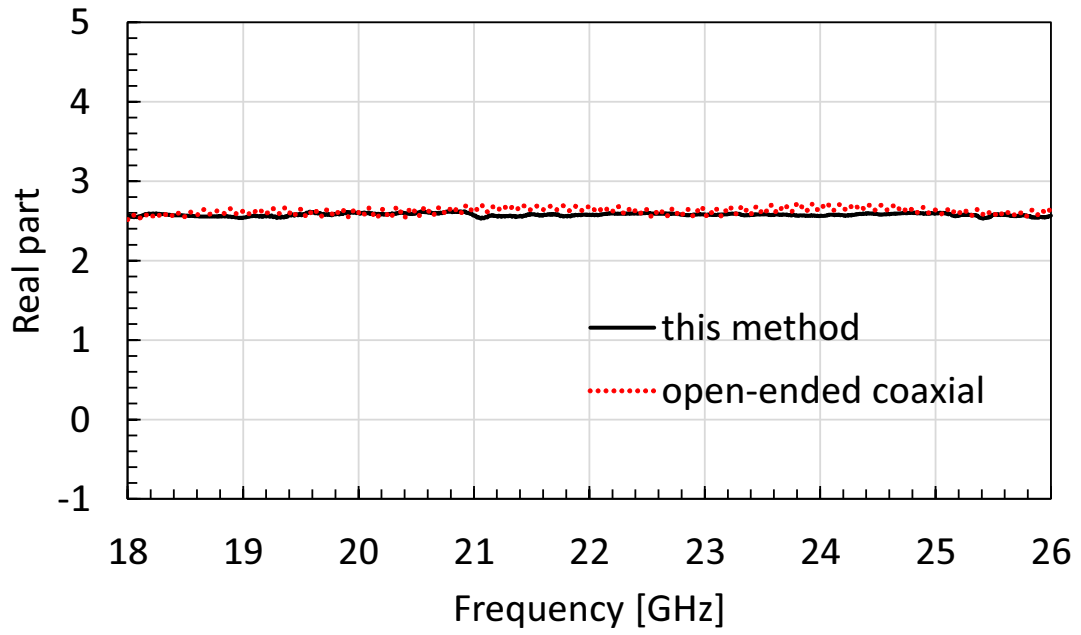


(a) Real parts of ϵ_r

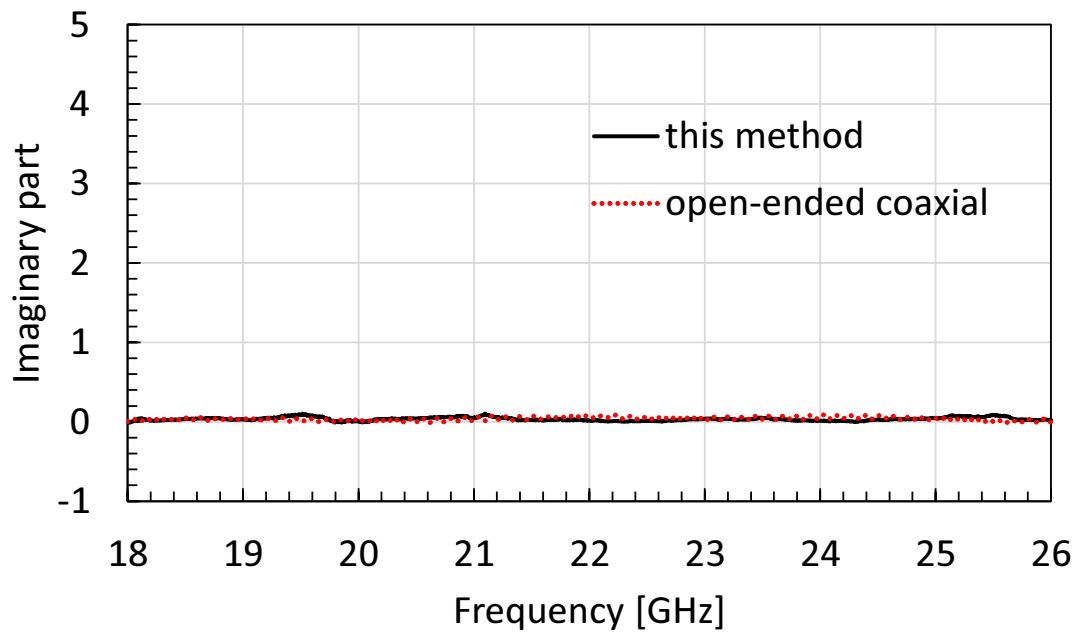


(b) Imaginary parts of ϵ_r

Figure 4.10: Relative permittivity ϵ_r extracted from a nylon cuboid ($2a = 2b = 100.0$ mm, $2c = 29.0$ mm) at 23.0°C .

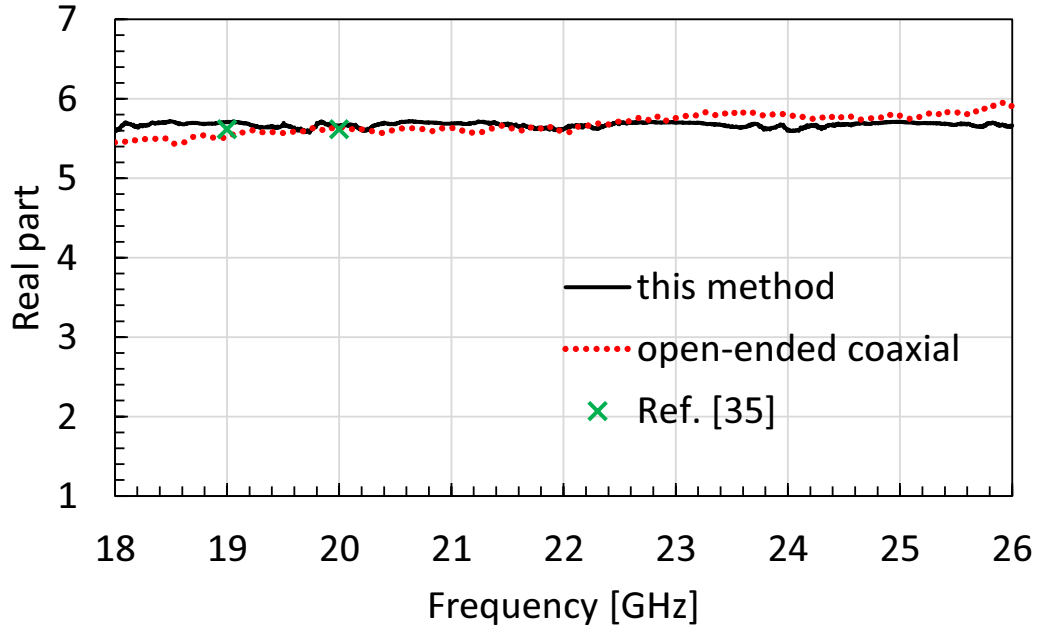


(a) Real parts of ϵ_r

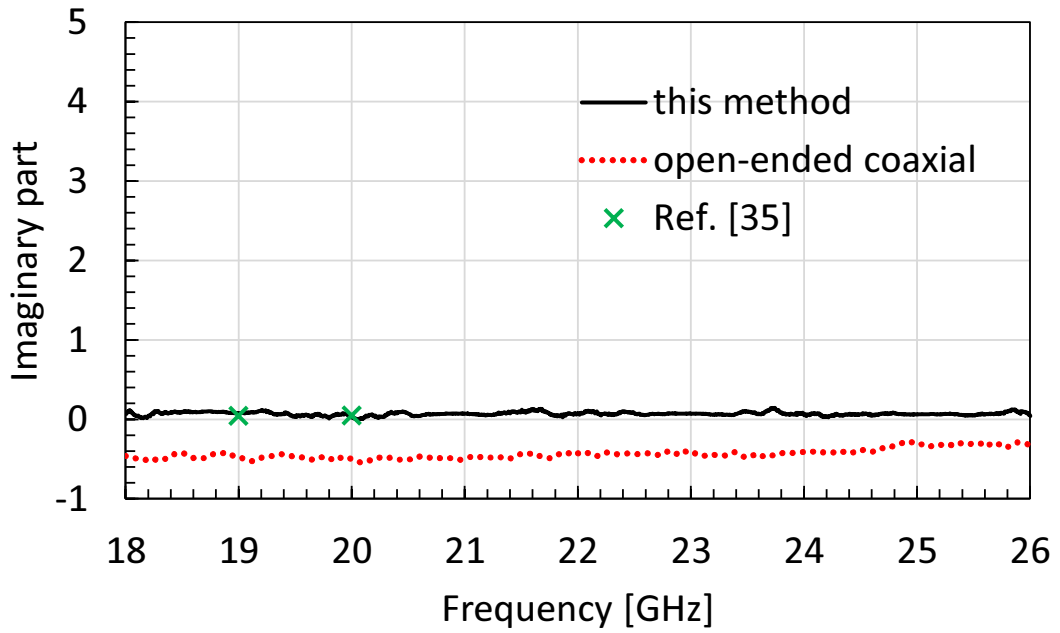


(b) Imaginary parts of ϵ_r

Figure 4.11: Relative permittivity ϵ_r extracted from an acrylic cuboid ($2a = 2b = 100.0$ mm, $2c = 30.0$ mm) at 23.0°C .



(a) Real parts of ϵ_r



(b) Imaginary parts of ϵ_r

Figure 4.12: Relative permittivity ϵ_r extracted from a Macor ceramic cuboid ($2a = 2b = 100.0$ mm, $2c = 30.0$ mm) at 21.0°C .

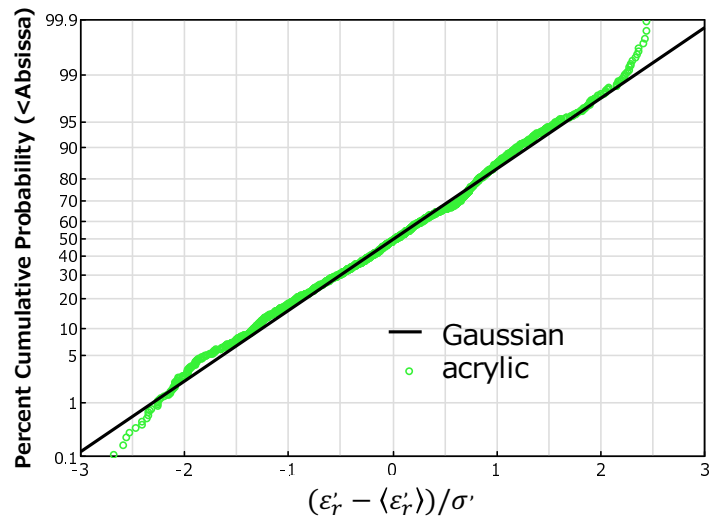


Figure 4.13: Percent cumulative probability distribution of the real part of the relative permittivity of measured acrylic sample.

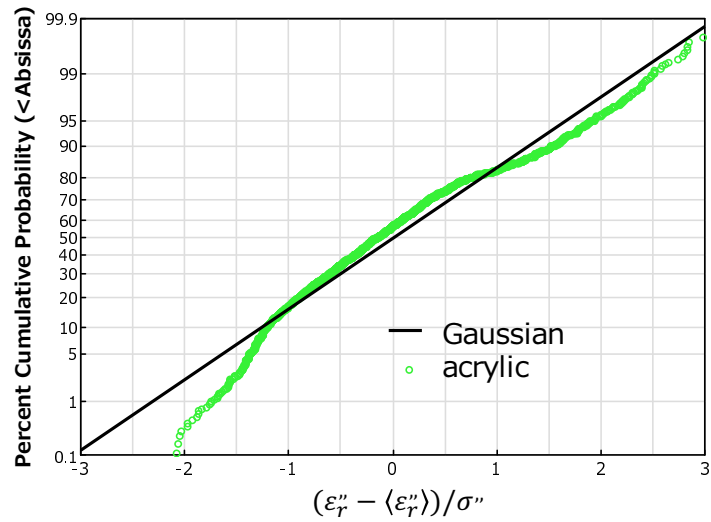


Figure 4.14: Percent cumulative probability distribution of the imaginary part of the relative permittivity of measured acrylic sample.

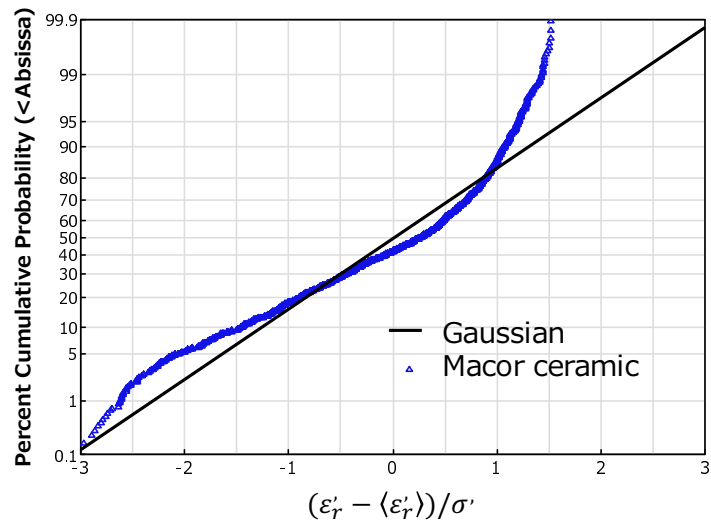


Figure 4.15: Percent cumulative probability distribution of the real part of the relative permittivity of measured Macor ceramic sample.

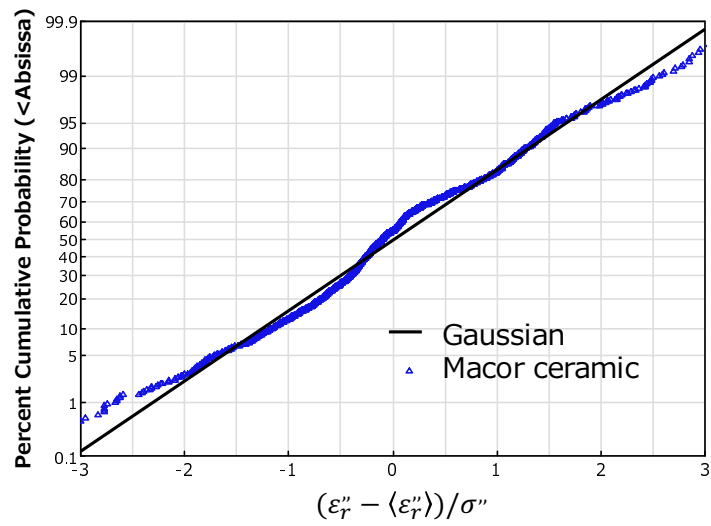


Figure 4.16: Percent cumulative probability distribution of the imaginary part of the relative permittivity of measured Macor ceramic sample.

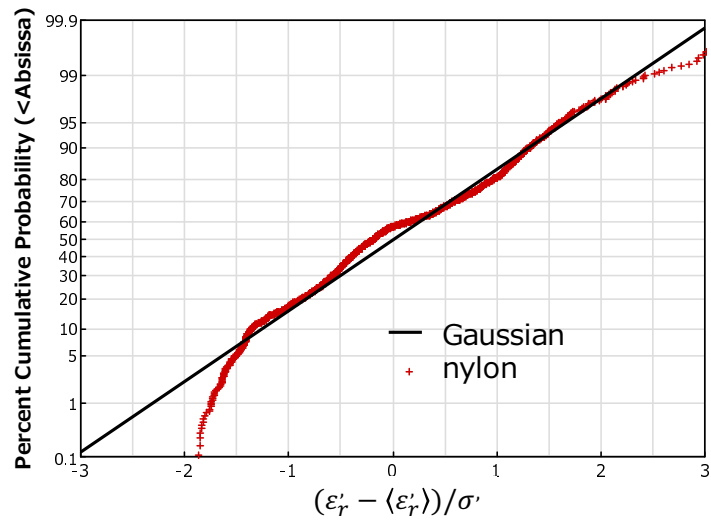


Figure 4.17: Percent cumulative probability distribution of the real part of the relative permittivity of measured nylon sample.

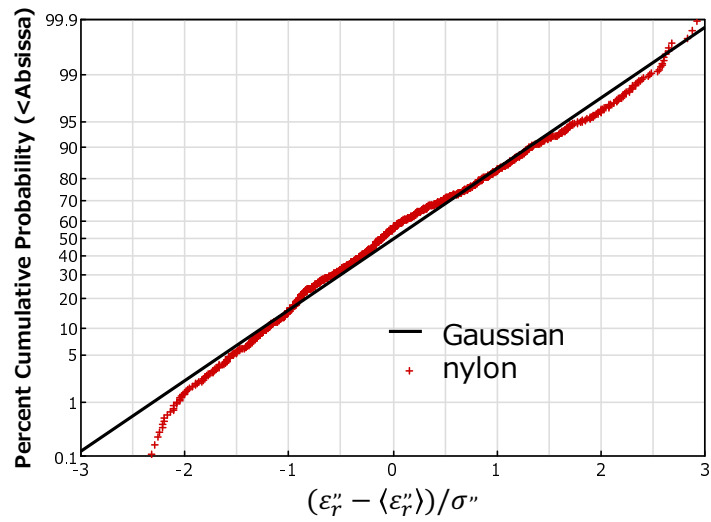


Figure 4.18: Percent cumulative probability distribution of the imaginary part of the relative permittivity of measured nylon sample.

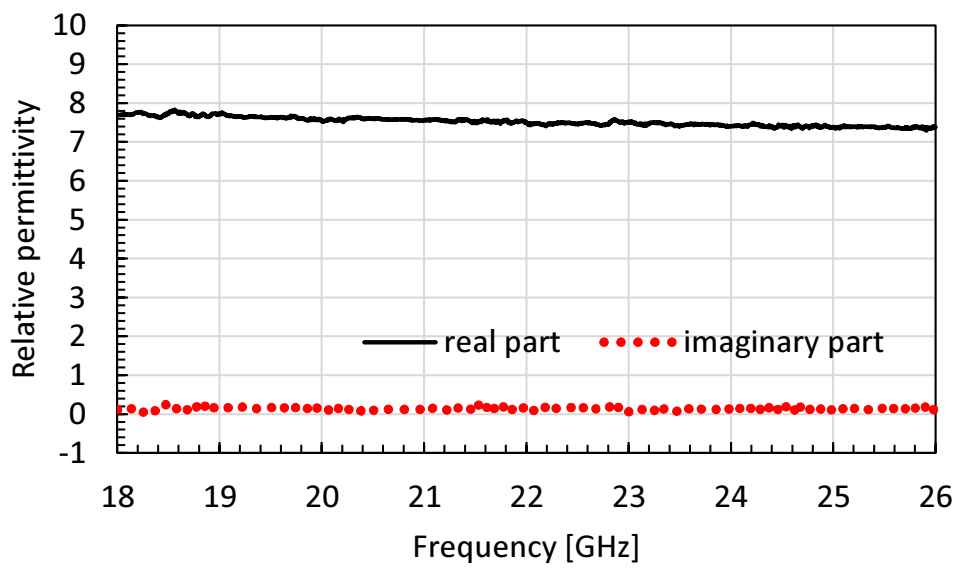


Figure 4.19: Relative permittivities extracted from a rubber cuboid.

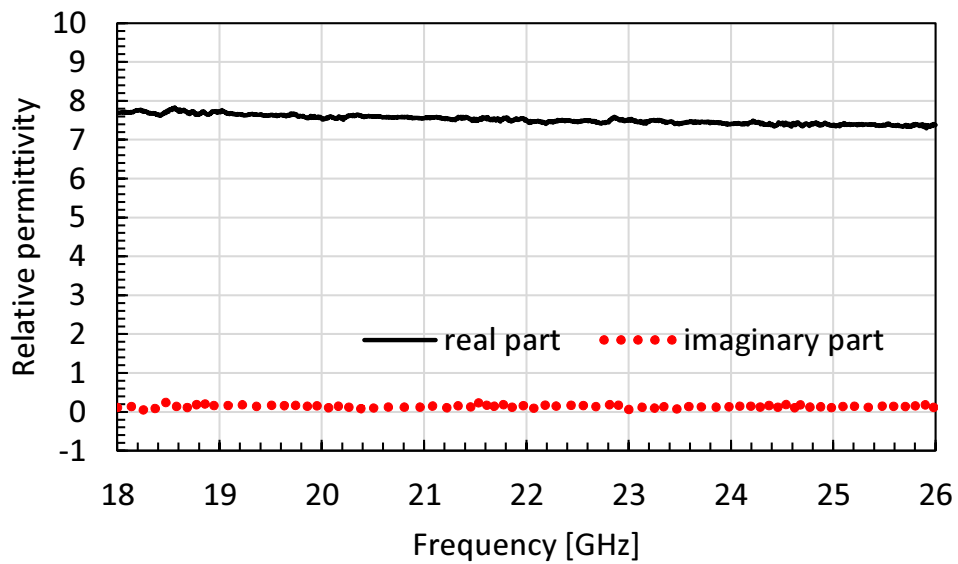


Figure 4.20: Relative permittivities extracted from a glass cuboid cuboid.

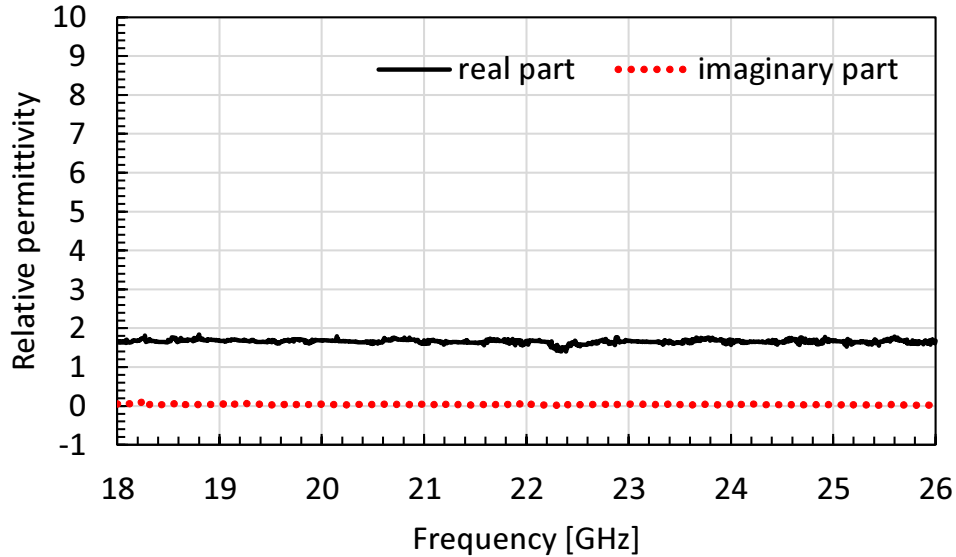


Figure 4.21: ε_r extracted from a wood cuboid ($2a = 2b = 2c = 120.0$ mm).

4.5 Conclusions

This chapter has proposed a free space method to estimate complex dielectric relative permittivity of homogeneous, isotropic non-magnetic solid materials. By using the multiple reflection coefficient extracted from complex scattering quantity in the normal reflection direction, complex dielectric relative permittivity of a sample material was estimated numerically over a broad range of frequency. An algorithm was developed to deal with the multi-value problem in solving for the complex relative permittivity. In order to secure a stable performance, the thickness of a sample material is suggested to follow the thickness requirement described by Eq. (4.8). Results obtained by this method were compared with results by the commercial open-ended coaxial probe method and the reference values [35]. Good agreements between our method and references have been observed for nylon and acrylic samples. Some relative dielectric permittivity results estimated from other samples also were presented. This method shows an attractive potential in dealing with both low and high contrast dielectric materials.